Modeling of Submillimeter Passive Remote Sensing of Cirrus Clouds

K. FRANKLIN EVANS

Program in Atmospheric and Oceanic Sciences, University of Colorado, Boulder, Colorado

STEVEN J. WALTER

Jet Propulsion Laboratory, California Institute of Technology, Pasadena, California

ANDREW J. HEYMSFIELD

National Center for Atmospheric Research, Boulder, Colorado

MERRITT N. DEETER

Program in Atmospheric and Oceanic Sciences, University of Colorado, Boulder, Colorado

(Manuscript received 28 January 1997, in final form 2 July 1997)

ABSTRACT

The scattering properties of cirrus clouds at submillimeter-wave frequencies are analyzed and characterized in this paper. This study lays a theoretical foundation for using radiometric measurements to investigate and monitor cirrus properties from high-flying aircraft or satellite. The significance of this capability is that it would provide data on the global distribution of cloud ice mass that is currently required to validate climate models. At present, these needs remain unmet by existing and planned observational systems.

In this study the brightness temperature depression (ΔT_b) of upwelling radiation due to cirrus clouds is simulated at 150, 220, 340, 500, 630, and 880 GHz. The effects of a range of size distributions, eight ice particle shapes, and different atmospheric profiles are modeled. The atmospheric transmission is high enough in the submillimeter windows to allow upper-tropospheric sensing from space, but absorption by water vapor reduces the sensitivity to lower cirrus clouds in a simply predictable manner. It is shown that frequencies above 500 GHz have adequate sensitivity to measure cirrus cloud properties. For these higher frequencies, the ΔT_b is closely proportional to ice water path (IWP) for median mass equivalent sphere diameters (D_{me}) above 125 μm. The differing sensitivity with frequency allows two channels to determine particle size.

A two-channel Bayesian algorithm is developed to assess retrieval accuracy with a Monte Carlo error analysis procedure. Particle shape, size distribution width, and receiver noise are considered as error sources. The rms errors for a nadir view with 630/880 GHz are less than 40% for IWP > 5 g m^{-2} and $D_{me} > 100$ μm, while using an oblique viewing angle of 73° results in the same accuracy down to an IWP of 1 g m^{-2} (visible optical depth less than 0.1). The two-channel algorithm and error analysis methods are used to show how submillimeter radiometer and millimeter radar measurements may be combined.

1. Introduction

The high altitudes and cold temperatures of cirrus clouds contribute to their distinct radiative properties as well as their resistance to adequate characterization. The cold brightness temperatures of cirrus clouds compared to clear skies means they provide a large infrared ''greenhouse'' effect in addition to reflecting solar flux. Numerical studies have shown that the optical thickness of cirrus clouds determines whether they warm or cool the atmosphere and surface (Stephens and Webster 1981; Platt 1981; Liou 1986). In addition, cirrus clouds cover a substantial fraction of the earth. The International Satellite Cloud Climatology Project (ISCCP, Rossow and Schiffer 1991) results for 1990 show that 18% of the globe on average is covered by high cloud not categorized as deep convection. Using the CO_2 slicing technique with infrared sounder data, Wylie et al. (1994) derive a 20% frequency for clouds above 400 mb with effective emissivities less than 0.95.

Because of their prevalence and radiative significance, it is crucial that cirrus clouds be accurately represented in climate models. GCMs now have improved cloud parameterizations that predict cloud ice mass (e.g., Fowler et al. 1996) as one part of the hydrologic cycle. Along with cloud fraction and optical properties,

Corresponding author address: K. Franklin Evans, Program in Atmospheric and Oceanic Sciences, University of Colorado, Campus Box 311, Boulder, CO 80309.
E-mail: evans@nit.colorado.edu

it is now important for cirrus ice mass distribution to be measured accurately for climate model evaluation. Current ice cloud parameterizations are hardly constrained by existing measurements of ice mass with error bars perhaps as large as a factor of 3.

The high altitude of cirrus clouds makes in situ measurements of microphysical properties difficult, and so they remain poorly known. In addition, the nonspherical shapes of the ice particles have made interpretation of remotely sensed observations subject to large error. For example, solar reflectance techniques for cirrus must convert reflectance to optical depth using phase functions that are highly sensitive to particle shape. Then, additional errors are introduced when optical depth is converted to ice water path with inferred effective particle sizes. Furthermore, there are substantial errors from vertical and horizontal inhomogeneities in clouds that are not optically thin. It is thus desirable to develop remote sensing techniques that will improve the measurement of cirrus characteristics such as integrated ice mass.

At submillimeter frequencies (greater than 300 GHz) the lower atmosphere emits a relatively uniform flux of upwelling radiation (the surface is unimportant because water vapor absorption makes the lower atmosphere opaque). Cirrus ice particles scatter some of this upwelling radiation downward. To an observer above a cirrus cloud, the scattering decreases the brightness temperature from the clear-sky value, while to an observer flying just below a cirrus cloud, the effect is to increase the brightness temperature. As the wavelength of microwave radiation decreases toward the sizes typical of cirrus particles, the sensitivity to cirrus ice mass increases dramatically. The change in brightness temperature depends on the integrated ice mass (ice water path or IWP) and the characteristic particle size and shape.

Passive microwave, particularly submillimeter wave, remote sensing has a number of potential advantages that complement existing visible and infrared techniques. Since the wavelength of submillimeter radiation is comparable to the size of ice particles in cirrus clouds, observed brightness temperature changes from cirrus are well correlated to ice mass. This contrasts with visible and infrared methods, which operate in the geometric optics limit where the signal is proportional to the particle area. Microwave radiation interacts with ice particles primarily through scattering so that cloud emission and temperature are relatively unimportant. Furthermore, radiative transfer tends to occur in a linear regime where the signal is directly proportional to the microwave optical depth. This reduces the importance of cloud inhomogeneity because the signal is proportional to the average cirrus properties in the field of view.

With advances in microwave detectors, the sensing of cirrus clouds with submillimeter radiometers is becoming practical. The millimeter-wave imaging radiometer (MIR) (Racette et al. 1996) that has flown on the NASA ER-2 has frequencies up to 325 GHz. The Odin satellite (a joint effort of Sweden, Canada, Finland, and France) is due to be launched in 1998 and will observe both astronomical objects and the earth's upper atmosphere. Odin will carry a submillimeter spectrometer capable of scanning the atmosphere at frequencies centered at 118, 495, 550, 555, and 572 GHz. A prototype submillimeter radiometer designed to measure cloud ice has been built at the Jet Propulsion Laboratory (JPL) and was flown on the NASA DC-8 in the fall of 1996.[1] The JPL radiometer measures two orthogonal linear polarizations at 500 and 630 GHz with matched 3° beamwidths.

Previous work examining microwave remote sensing of cirrus has been limited. Gasiewski (1992) performed a theoretical study on the use of radiometric measurements from 90 to 410 GHz. Using radiative transfer simulations, he investigated the sensitivity of brightness temperatures to water vapor, precipitation, liquid clouds, and ice clouds (modeled with a one-parameter size distribution of spheres). He showed that multiple, widely spaced frequencies provided additional degrees of freedom for cloud sensing. Muller et al. (1994) performed a similar theoretical study at frequencies used by the advanced microwave sounding unit (AMSU) and used a single size distribution of ice spheres.

This study extends the theoretical work of Evans and Stephens (1995b) to submillimeter frequencies and characterizes the retrieval error using a preliminary two-channel algorithm. The previous work with frequencies up to 340 GHz found that the sensitivity of microwave radiometry to cirrus IWP increases with frequency and that characteristic particle size is the major factor in relating brightness temperature change to IWP. The differential sensitivity of two widely spaced radiometer frequencies was found to be useful in estimating characteristic particle size. The brightness temperature depression was shown to be nearly independent of cloud temperature and details of the underlying atmosphere. The purpose of this study is to calculate radiative properties for a range of realistic cirrus clouds at six frequencies emphasizing the higher submillimeter frequencies. An algorithm to retrieve cirrus IWP and particle size is presented. This allows the effects of various error sources (such as receiver noise, particle shape, water vapor absorption, and background variations) on the retrieval accuracy to be investigated.

Modeling methods are covered in section 2. The use of observed ice cloud particle size distributions is described in section 3. The basic radiative transfer modeling results for gamma distributions are presented in section 4. Section 5 describes the retrieval algorithm and error analysis for the submillimeter ra-

[1] Data from these measurements are currently being analyzed and will be reported at a later date (S. Walter).

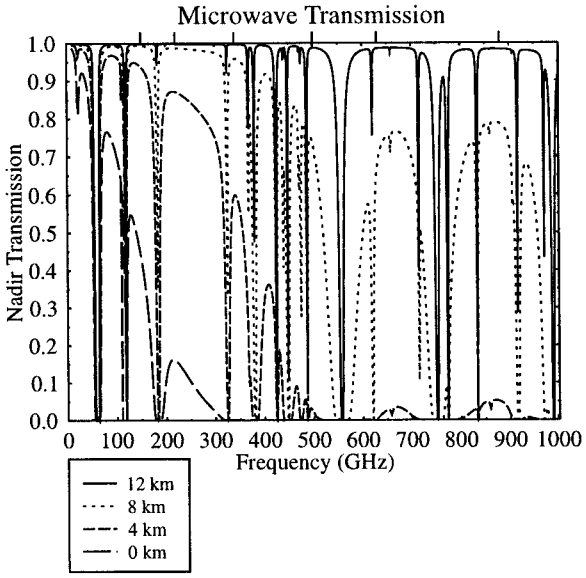

FIG. 1. Transmission from space to 12, 8, 4, and 0 km in a standard midlatitude summer atmosphere. The six modeling frequencies (150, 220, 340, 500, 630, and 880 GHz) are indicated at the top. The integrated water vapor amounts from space to the four altitudes are 0.011, 0.314, 3.28, and 29.5 kg m^{-2}.

diometer algorithm and a combined radar–radiometer technique.

2. Modeling methods

The modeling results are calculated for six frequencies: 150, 220, 340, 500, 630, and 880 GHz. These frequencies are located in atmospheric transmitting windows and were chosen to coincide with frequencies used either by existing sensors or candidates for future instruments. The MIR has channels at 150 and 220 GHz and three channels spaced around the water vapor line at 325 GHz. The JPL prototype ice cloud radiometer made measurements at 500 and 630 GHz. These two frequencies were originally selected based on the availability of existing receivers and were not optimized for cirrus sensing. The 880-GHz frequency was chosen to be in the center of an even higher frequency atmospheric window.

The atmospheric transmission from space to four altitudes in the atmosphere is shown in Fig. 1. The lowest two frequencies have significant transmission to the surface, while the three highest frequencies have adequate transmission to the upper troposphere and no contribution from the lower troposphere. The transmission is strongly dependent on the humidity of the atmosphere.

To simulate brightness temperatures measured by a submillimeter radiometer, it is necessary to 1) model single scattering properties of distributions of realistic cirrus ice particles and 2) model polarized radiative transfer in atmospheres containing a range of cirrus cloud properties.

TABLE 1. The maximum extent L, rosette bullet diameter h, column diameter h, and dipole size d for the 21 discrete cirrus particle sizes.

Length L (μm)	Rosette h (μm)	Column h (μm)	Dipole size d (μm)
10	4	6	8
13	4	8	8
16	5	9	8
20	6	11	8
25	8	13	8
32	9	16	8
40	11	19	8
50	13	23	8
63	16	28	8
79	19	33	8
100	23	40	8
126	28	48	8
158	33	58	8
200	40	70	10
251	48	84	13
316	58	100	15
398	69	121	19
501	83	145	23
631	100	175	28
794	121	210	34
1000	145	252	42

a. DDA modeling

The electromagnetic scattering properties of cirrus ice particles are computed here using the discrete dipole approximation (DDA). For a recent review of the method, see Draine and Flatau (1994). The DDA approach divides the particle into a number of subunits (dipoles) whose size is small compared to the incident wavelength of radiation. The main computational task of the DDA is to invert the coupled system of dipole interactions to give the dipole polarizations from which the resulting far-field scattering properties are derived. DDA is a general technique because it can be applied to any particle shape, although computer limitations have restricted the method to particles that are only slightly larger than the wavelength. The method used here is based on that of Goedecke and O'Brien (1988) and is described in detail in Evans and Stephens (1995a) [except that the isotropic lattice dispersion relation (Draine and Goodman 1993) is used in this study for the dipole self-interaction term].

The DDA is used to model the scattering properties for 21 particles sizes from 10 to 1000 μm (1 mm) in particle diameter. In situ observations of cirrus show that particles larger than 1.0 mm comprise a very small (if any) percentage of the total particle population, although this depends on how the boundary between cirrus and thicker precipitating ice clouds is defined. Particle sizes smaller than 10 μm, even if they exist in most cirrus clouds, usually have very little effect on either the submillimeter radiation or the ice water content. The DDA dipole size varies with the particle size (Table 1). The dipole size criterion $|m|kd$ ($k = 2\pi/\lambda$, λ is the wavelength, and d is the dipole size) for the largest dipole size and highest frequency does not exceed 1.4. This implies that the DDA dipole discretization is reliable.

TABLE 2. The eight particle shapes modeled with the volume fraction given.

Shape	Vol fraction	Description
coln	1.0	Solid column
colh	1.0	Hollow column (hourglass)
cold	0.65	Low-density column
rs4o	1.0	Four bullet rosettes
rs5o	1.0	Five bullet rosettes
rs7o	1.0	Seven bullet rosettes
stik	0.65	Stick-ball
sphr	1.0	Sphere

The index of refraction for ice (m) at the six frequencies is obtained from Warren (1984).

The most uncertain aspect of modeling the submillimeter scattering properties of cirrus particles is that of shape. While some characteristic shapes, such as columns and bullet rosettes occur frequently, the properties of individual rosettes vary widely, and irregular shapes are often more common (Kikuchi 1968; Mitchell 1994). Thus, one cannot hope to model cirrus particle shapes exactly but can choose a set of realistic shapes that provide a range of scattering properties. Table 2 lists the eight particle shapes modeled here: three types of columns, three bullet rosettes, and two irregulars. The columns are modeled as cylinders, rather than hexagonal columns, because the submillimeter wavelengths cannot resolve the fine details (less than 50 μm). The hollow column is a cylinder with cones removed from each end. The spatial rosettes are modeled as cylindrical bullets emanating from the crystal center with the bullets maximally separated. Hexagonal plates are not modeled as they are infrequently observed for the temperatures considered (less than -20°C). Particles classified as irregular in microphysical observations are often sublimated crystals and tend to be rounded and elongated with some protrusions (otherwise, they would be classified as spheres, columns, or rosettes). The ''stick-ball'' particle shape is a cylinder attached to a sphere of 40% of the particle length and is meant to simulate one type of irregular particle. Spheres are a particularly unrealistic shape for large cirrus particles and are mainly used for comparison to the other shapes.

One major uncertainty in modeling cirrus particles is that of density. Clearly, when using spheroidal shapes to model crystals, it is necessary to model the particles as an ice–air mixture with a density less than solid ice and which is presumably dependent on size. Pristine shapes, such as columns, hollow columns, and bullet rosettes, would be expected to have grown as solid ice through vapor deposition. Since the DDA can model the detailed morphology of these shapes, the density is made of solid ice. The irregular particles, which are modeled with an approximate shape, should have a reduced density. Some of the particle shapes were modeled with a reduced density of 0.60 g cm^{-3} (Table 2) using the Lorentz–Lorenz mixing rule for an ice–air mixture.

Empirical studies indicate that vapor deposition causes ice crystals to become elongated (the c to a axis length ratio increases) as they grow larger. Thus, the aspect ratio of the particles, or the bullets for rosettes, varies with particle size. A power-law formula is chosen for the aspect ratio [$\phi = 2.5(L/100\ \mu\text{m})^{0.20}$, where L is the maximum dimension], which is within the range of published empirical cirrus aspect ratios (e.g., Heymsfield 1972). This results in an aspect ratio of 1.58 at 10 μm, 2.50 at 100 μm, and 3.96 at 1000 μm.

All the shapes except spheres are assumed to have a preferred orientation. Aerodynamic forces tend to cause the long axes of larger particles to fall horizontally. Laboratory studies (Ono 1969), lidar observations (Platt et al. 1978), and theoretical modeling (Klett 1995) indicate that regular hexagonal particles (larger than 20 μm according to Klett) fall within a few degrees of this horizontal orientation. For the nonrosette shapes, the long axis is oriented randomly in the horizontal plane, while rosettes are randomly oriented in the horizontal plane but with one bullet pointing down. Four other shapes (including two with an alternate aspect ratio formula—a randomly oriented rosette and a prolate spheroid) were modeled but were found to have substantially similar radiative properties and so are not included here.

The matrix inversion method of solving the DDA coupled dipole system is used for these simulations (Evans and Stephens 1995a). The scattering properties are computed for eight discrete zenith angles per hemisphere chosen with the Lobatto quadrature scheme. The azimuthal orientation averaging is done with eight incident azimuth angles over 180°. Tests indicated that this level of angular discretization gave negligible error for the largest size parameter.

b. Polarized radiative transfer model

The extinction and scattering matrices and emission vector computed by the DDA model are combined with a weighted average over the 21 particle sizes to produce scattering properties for a variety of size distributions (section 2c). The gaseous absorption for the atmospheric profile is computed by the MPM92 (Millimeter-wave Propagation Model 1992) developed by Liebe (1989).

The polarized radiative transfer model described in Evans and Stephens (1995b) is used to compute radiances. This is a monochromatic plane-parallel model that uses the doubling–adding method for solving the discrete angle radiative transfer system. The azimuthally symmetric geometry implies that only the I and Q Stokes parameters are non-zero, thus the radiation is linearly polarized and can be fully described by vertical (V) and horizontal (H) components. The polarized radiative transfer model was modified to compute the radiance at any model level in the atmosphere. The model always uses the Planck function during the radiative transfer procedure, even when converting to brightness

temperature, rather than allowing the Rayleigh–Jeans approximation.

The issue of how to represent the modeled radiance in terms of brightness temperature becomes a particular concern for the upward-looking geometry. The effective blackbody (EBB) brightness temperature is that obtained by inverting the Planck function, while the Rayleigh–Jeans brightness temperature is derived from the low-frequency limit of the Planck function in which temperature and radiance are linearly related. It is desirable to use a brightness temperature definition that is linearly related to radiance. For radiances typical of the downward-looking geometry, the EBB brightness temperature is still linear in the radiance for submillimeter frequencies. For brightness temperatures above about 50 K, the EBB and Rayleigh–Jeans brightness temperatures are related by a constant, frequency-dependent offset (21.1 K at 880 GHz) where

$$T_{\mathrm{RJ}} \approx T_{\mathrm{EBB}} - (0.0240 \text{ K GHz}^{-1})\nu. \qquad (1)$$

However, for submillimeter frequencies, the EBB brightness temperature is no longer linearly related to the radiance for upward-looking geometries, which have very low radiance. The Rayleigh–Jeans brightness temperature is chosen here because it is linear and goes to 0 K at zero radiance. The Rayleigh–Jeans brightness temperatures will give the same brightness temperature *differences* as the linear brightness temperatures that result from a standard radiometer calibration with blackbody sources.

c. Modeling procedures

As in previous modeling studies (Evans and Stephens 1995a), gamma distributions are used to generate size distributions of cirrus ice particles. Gamma distributions are specified by three parameters and so have the flexibility to represent a desired ice water path, characteristic particle size, and width of the distribution. As shown below, gamma distributions represent the aspects of particle size distributions that are relevant for submillimeter radiative transfer quite well. A major departure from the previous work is that the equivalent mass diameter, and not the maximum particle dimension, is the basis for the size distribution. The concentration $N(D)$ of particles of size D is

$$N(D) = aD_e^{\alpha} \exp[-(\alpha + 3.67)D_e/D_{\mathrm{me}}], \qquad (2)$$

where D_e is the diameter of the equivalent mass sphere and D_{me} is the median mass diameter of the distribution. The value of D_e depends not only on the particle diameter D but also on its shape and density. The width of the distribution is set by α, and a is found from the ice mass content. Compared to the maximum particle diameter, the equivalent diameter is more suited for submillimeter radiometry and is used extensively in the radar community. This definition of the characteristic particle size D_{me} is the same as that used by Matrosov et al. (1994) (their D_m). The equivalent mass diameter reduces the microwave radiative differences between particle shapes to those based purely on morphology, independent of volume. The relation between D_{me} and other measures of particle size depends on shape and α, but for solid spheres with $\alpha = 1$, $D_{\mathrm{me}} = 2.3r_e$, where r_e is the effective radius.

The scattering properties of the gamma size distributions are computed from a weighted average of the scattering properties of the 21 discrete particle sizes. The weights are derived from (2) using an interpolation procedure (Evans and Stephens 1995a). The modeling varies the ice water path from 1 to 1000 g m^{-2} in approximately 2-dB steps with the median equivalent diameter ranging from 40 to 400 μm in approximately 1-dB steps. It should be noted that because the gamma distribution is truncated at the largest particle length of 1000 μm, the highest D_{me} parameters used here are larger than the true median mass diameter of the resulting distribution. The largest discrepancy due to truncation between the specified gamma distribution D_{me} and that found from fitting the second and sixth moments (section 3a) occurs for the largest size ($D_{\mathrm{me}} = 400$ μm) and widest distribution ($\alpha = 0$) for the stick-ball shape where the fitted D_{me} is 239 μm. The truncation effect is small for values of D_{me} below about 200 μm.

The brightness temperatures observed by the simulated radiometer are computed with the multistream polarized radiative transfer model. The modeled atmosphere is divided into 0.5-km layers between 0 and 40 km. The surface, which is generally unimportant because of the negligible transmission at submillimeter wavelengths, is modeled as a Lambertian surface with an emissivity of 0.95. The cosmic background radiation is negligible at submillimeter frequencies although it is included. The radiances are converted to vertically and horizontally polarized Rayleigh–Jeans brightness temperatures and output at the eight discrete Lobatto zenith angles per hemisphere.

Brightness temperatures computed for a cloud-free atmosphere are subtracted from those calculated with a cirrus cloud to get the brightness temperature difference ΔT_b. Because cirrus clouds are usually optically thin in the submillimeter, the brightness temperature difference is proportional to the ice water path for all other properties fixed. Thus, it is appropriate to characterize the effect of cirrus with a normalized brightness temperature difference obtained by dividing by the ice water path (ΔT_b/IWP). This quantity will be referred to as the ''sensitivity.'' The ice water path used to normalize the brightness temperature takes into account the longer pathlength for oblique angles. The sensitivity shown is computed for the lowest IWP that results in $\Delta T_b > 1.0$ K.

Climatological lidar data from Virginia (Winker and Vaughan 1994) indicate that cirrus clouds are mostly geometrically thin with a mean thickness near 1 km. Thus, all the cirrus clouds modeled here are 1-km thick (it is the IWP that really matters). Previous work (Evans

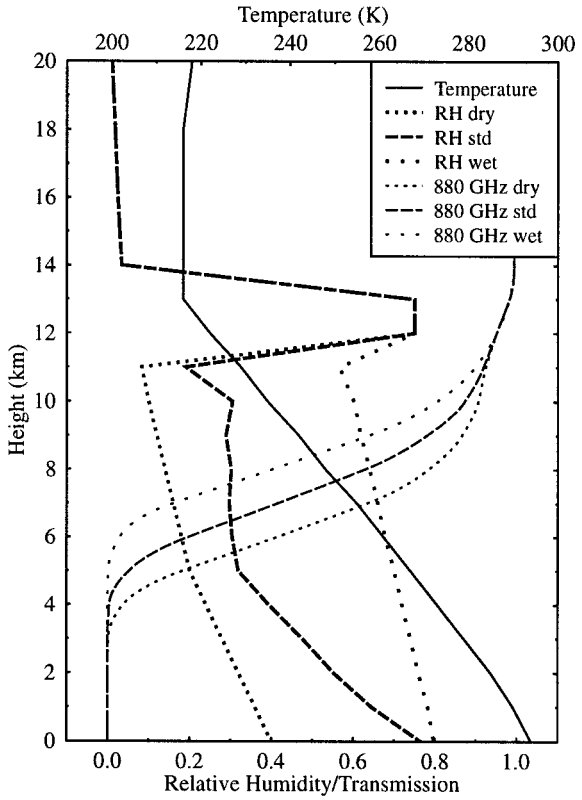

FIG. 2. Profiles of temperature, relative humidity, and 880-GHz transmission to space for the standard midlatitude summer atmosphere and for drier and moister ones.

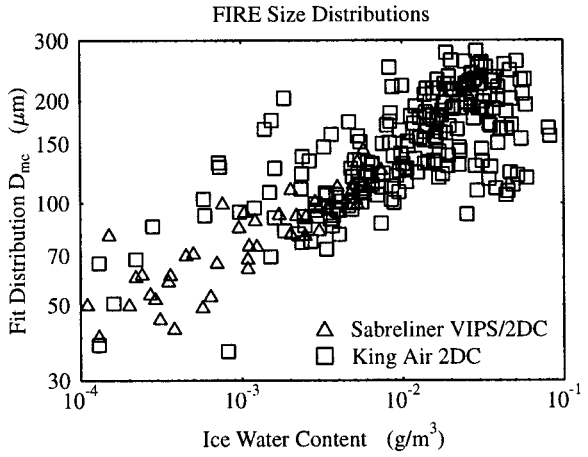

FIG. 3. The median mass equivalent particle diameter fitted to observed ice cloud size distributions using the second and sixth moments as a function of ice water content. Included are 50 VIPS/2-DC distributions from the Sabreliner aircraft and 227 2D-C distributions from the King Air aircraft during FIRE II.

and Stephens 1995b) showed that the microwave radiative characteristics of cirrus clouds were insensitive to the underlying atmosphere. Most of the modeling here uses a standard midlatitude summer atmosphere with cirrus from 12 to 13 km (tropopause is 13 km). The relative humidity with respect to water of the cirrus layer is always set to 75%. The profiles of temperature, relative humidity, and 880-GHz transmission to space are shown in Fig. 2. The transmission is high (greater than 0.8) for much of the upper troposphere, but ice clouds can be found at levels where the transmission is not very high (see section 5b for a discussion of these effects). Brightness temperatures are output for two ''flight levels,'' or heights in the atmosphere, one for upwelling radiance above the cloud and one for downwelling radiance below the cloud. (For the summer cases, the levels are 20 and 10 km, corresponding to typical flight altitudes for the NASA ER-2 and DC-8 research aircraft.)

3. Modeling with observed cirrus distributions

Observed particle size distributions are used for model runs presented in this section. Two sets of cirrus particle size distributions were obtained from aircraft during the FIRE II experiment in 1991 in Kansas. The first set is a composite distribution measured on the Sabreliner aircraft with the Video Ice Particle Sampler (VIPS) (McFarquhar and Heymsfield 1996) and the 2D-C probe. The second set was measured on the King Air aircraft with the 2D-C probe. The VIPS' probe measured particles down to 5 μm, the 2D-C probe on the Sabreliner down to 100 μm, and the 2D-C probe on the King Air down to 25 μm. The crossover point for the composite distributions is 100 μm (VIPS for smaller particles and 2D-C for larger ones). The composite size distributions from the Sabreliner have crystal habit (shape classification) information, while the King Air distributions have projected area ratio classifications. Data from the two most studied days of FIRE II, 26 November and 5 December, were chosen for this analysis. Because the VIPS' data were analyzed manually, only 50 size distributions (27 for 26 November and 23 for 5 December) were available for the Sabreliner size distributions. To reduce the number of distributions to be modeled, the 5-s samples of the King Air data were averaged over 60 s, which resulted in 227 distributions during cruising altitudes (152 for 26 November and 75 for 5 December).

The reason for using both sets of distributions is that the Sabreliner tended to fly in the upper parts of the cirrus clouds, biasing the sample toward smaller particles. The King Air flew lower in the clouds, sampling the higher ice water content (IWC) and larger particles, which are closer to the vertically integrated particle sizes. Figure 3 shows the median equivalent mass sphere diameter D_{me} as a function of the IWC obtained from the size distributions. The D_{me} is obtained from fitting the second and sixth moments (see next section). Both the Sabreliner and King Air data show a correlation between IWC and particle size. The Sabreliner particle sizes (D_{me}) are smaller than 150 μm, lying primarily

TABLE 3. Percentiles of fractional difference in radiative sensitivity between observed and gamma particle size distribution fitted with moment N and $\alpha = 1$.

Aircraft	Frequency	$N = 4$		$N = 5$		$N = 6$	
		50%	90%	50%	90%	50%	90%
Sabreliner	340	0.087	0.227	0.031	0.098	0.026	0.077
King Air	340	0.058	0.146	0.044	0.168	0.072	0.210
Sabreliner	630	0.041	0.140	0.043	0.097	0.069	0.149
King Air	630	0.035	0.103	0.055	0.126	0.074	0.154

between 40 and 120 μm, while the King Air D_{me} yields values from 75 to 300 μm.

a. Gamma distribution equivalence

The observed size distributions are used in radiative transfer calculations to determine whether gamma distributions can adequately represent real size distributions. This is done by fitting a gamma distribution to each observed distribution and calculating the radiative sensitivities from the observed and gamma distributions. If the sensitivities are very close, then the observed distributions are said to be equivalent to the fitted gamma distribution.

There are several ways in which gamma distributions could be fitted to the observed size distributions. A least squares approach could be used to fit the number concentration, but number concentration is not directly relevant for radiative transfer. Since the particle scattering/radiative transfer process is related to the broad characteristics of the size distribution, the approach taken here is to fit to moments of the observed D_e distribution. Two methods of obtaining the equivalent gamma distribution are implemented: 1) fix the parameter $\alpha = 1$ and calculate the median mass diameter D_{me} from one moment (the Nth) or 2) calculate both D_{me} and α from two moments (the $N1$th and $N2$th). In all cases, the gamma distribution is required to have the same mass content (equivalent to constraining the third moment). If M_N is the Nth moment of the equivalent diameter

$$M_N = \sum_i n_i D_{e,i}^N, \tag{3}$$

then α may be obtained by solving

$$\left(\frac{M_{N2}}{M_3}\right)^{1/(N2-3)} \left(\frac{M_3}{M_{N1}}\right)^{1/(N1-3)} = \left[\frac{\Gamma(\alpha + N2 + 1)}{\Gamma(\alpha + 4)}\right]^{1/(N2-3)} \left[\frac{\Gamma(\alpha + 4)}{\Gamma(\alpha + N1 + 1)}\right]^{1/(N1-3)}. \tag{4}$$

Given α, the median mass diameter is calculated from

$$D_{\text{me}} = (\alpha + 3.67) \left[\frac{M_{N1}}{M_3} \frac{\Gamma(\alpha + 4)}{\Gamma(\alpha + N1 + 1)}\right]^{1/(N1-3)}. \tag{5}$$

These formulas assume an untruncated gamma distribution.

For the fits performed here, the distributions with the largest particle sizes (D_{me}) have narrow distribution widths (high α). The resulting values of α range from a lower limit of -0.5 up to about 7 and are larger than those reported elsewhere (Kosarev and Mazin 1989) because higher order moments, rather than the number concentration, are being fitted.

To determine whether the gamma distributions derived from the observed size distributions are equivalent in a radiative sense, brightness temperatures at 340 and 630 GHz are computed from modeled cirrus clouds with observed and theoretical gamma size distributions. Cirrus clouds with either columns or five-bullet rosettes and an IWP of 10 g m^{-2} are modeled. Sensitivities (ΔT_b/IWP) are analyzed for five viewing angles/polarizations (0°, 26°V, 26°H, 49°V, 49°H) and both upward and downward viewing geometries.

The criterion for radiative equivalence is the absolute value of the fractional difference in sensitivity. The 50 and 90 percentiles of the fractional differences in sensitivity are shown in Tables 3 and 4. The first table shows the results where α was fixed at 1 and the ice mass and median equivalent diameter D_{me} were fitted. For the smaller particle distributions (Sabreliner) and the lowest frequency (340 GHz), the size parameter is small and the moment that provides the best fit is the sixth, which indicates that Rayleigh scattering dominates. When the particle sizes approach the submillimeter wavelengths, the best fitting moment is the fourth. This results in the observed and gamma distributions having sensitivities within 5% for half of the cases and within 15% for 90%

TABLE 4. Percentiles of fractional difference in radiative sensitivity between observed and gamma particle size distribution fitted with moments $N1$ and $N2$.

Aircraft	Frequency (GHz)	$N1 = 4$ $N2 = 6$		$N1 = 2$ $N2 = 6$	
		50%	90%	50%	90%
Sabreliner	340	0.000	0.037	0.000	0.077
King Air	340	0.022	0.059	0.051	0.126
Sabreliner	630	0.008	0.051	0.024	0.120
King Air	630	0.008	0.053	0.032	0.076

of the cases. Table 4 shows that even better submillimeter radiative equivalence can be achieved by fitting both D_{me} and α. If the fourth and sixth moments are fitted, then 90% of the cases have sensitivities within 6%. There are a few cases where using a fitted gamma distribution to represent an actual size distribution leads to larger errors. However, keep in mind that the submillimeter radiometry technique is for determining vertically integrated cirrus properties, and these integrated distributions will tend to be smoother and more regular than the local distributions.

The results in Tables 3 and 4 indicate that the submillimeter radiometry signal is proportional from the third to the fifth moment of the cirrus particle size distribution. This allows submillimeter radiometers to complement other sensors that are sensitive to different moments of the size distribution. Visible and infrared sensors are sensitive to the second moment and millimeter radars to the sixth moment. Results for these two moments yield a somewhat larger radiative error with 90% of the cases having sensitivities within 13%. Thus, the gamma distribution, fitted with the appropriate moments, should be able to represent cirrus observed with instruments spanning from visible to millimeter wavelengths.

b. Ice water path–ΔT_b relations

The size distributions observed during FIRE are further used to model the relation between brightness temperature differences (ΔT_b) and IWP: The ice crystal shape information is available for the Sabreliner VIPS/2D-C size distribution and so appropriate assignments are made from the NCAR crystal habit codes to four of the shapes modeled here (coln, rs5o, stik, sphr). Most of the crystal shapes identified in the VIPS distributions are quasi-spherical (sphr). Since only the area ratio classification is available for the King Air 2D-C probe, these distributions are simply modeled with the five bullet rosettes (rs5o). The cloud probe size distributions are assumed to give the number concentration of particles with a maximum length of the probe bin center.

The brightness temperature differences computed from the observed size distributions are shown for all six frequencies in Figs. 4 and 5. Since the Sabreliner data has smaller particles and lower ice water content, the ΔT_b's are quite small (under 4 K at 630 GHz) as compared to the King Air data. The Sabreliner points are also shifted to a higher ΔT_b at the highest frequencies because of the greater sensitivity of solid ice spheres that make up the bulk of the Sabreliner distributions, as compared to the sensitivity of rosettes. Since only one shape is modeled for the King Air distributions, the scatter is due to variations in characteristic particle sizes. Besides increased sensitivity, the scatter about a power law relation between IWP and ΔT_b is reduced at the higher frequencies. The reasons for these behaviors will be discussed later.

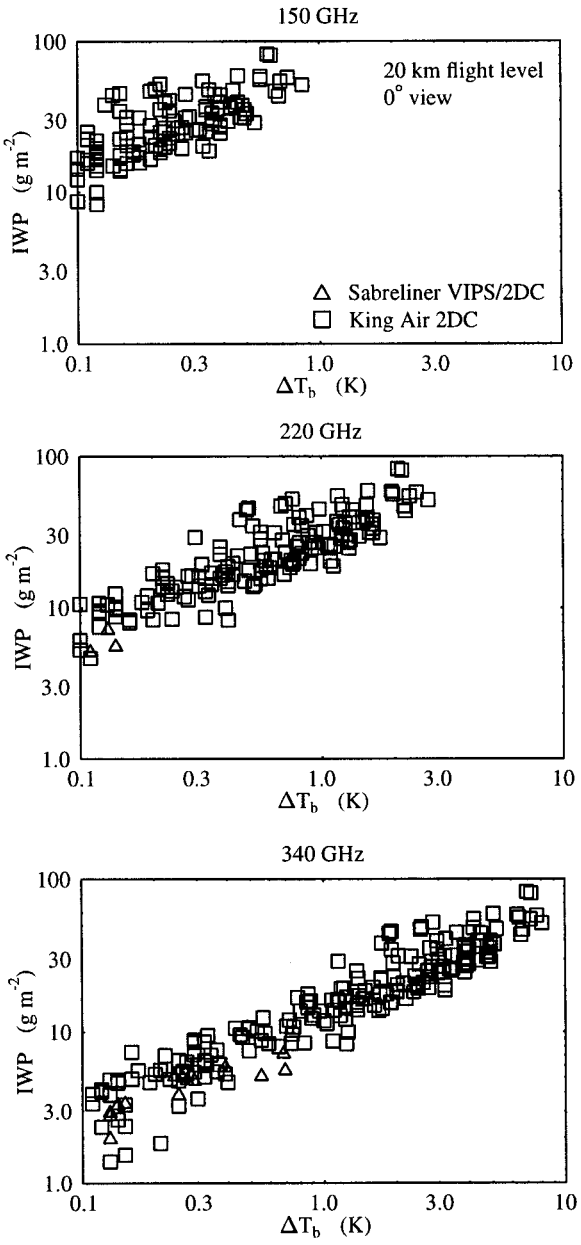

FIG. 4. Scatterplots of ice water path vs brightness temperature difference (ΔT_b) for 150, 220, and 340 GHz for ice cloud size distributions from FIRE II. The viewing geometry is from nadir (0°). The Sabreliner VIPS/2D-C distributions use the identified crystal shape, while the King Air 2D-C distributions use the five-bullet rosette shape.

These figures show that the ΔT_b for a given IWP increases dramatically with radiometer frequency. The largest ΔT_b is only 2.3 K at 150 GHz and 63 K at 880 GHz. A brightness temperature depression of $\Delta T_b = 1$ K (measurement noise of 0.5 K should be achievable) corresponds to IWPs of 49, 26, 12, 6, 4, 2 g m^{-2} for 150, 220, 340, 500, 630, and 880 GHz, respectively, showing the benefit of submillimeter frequencies for observing cirrus.

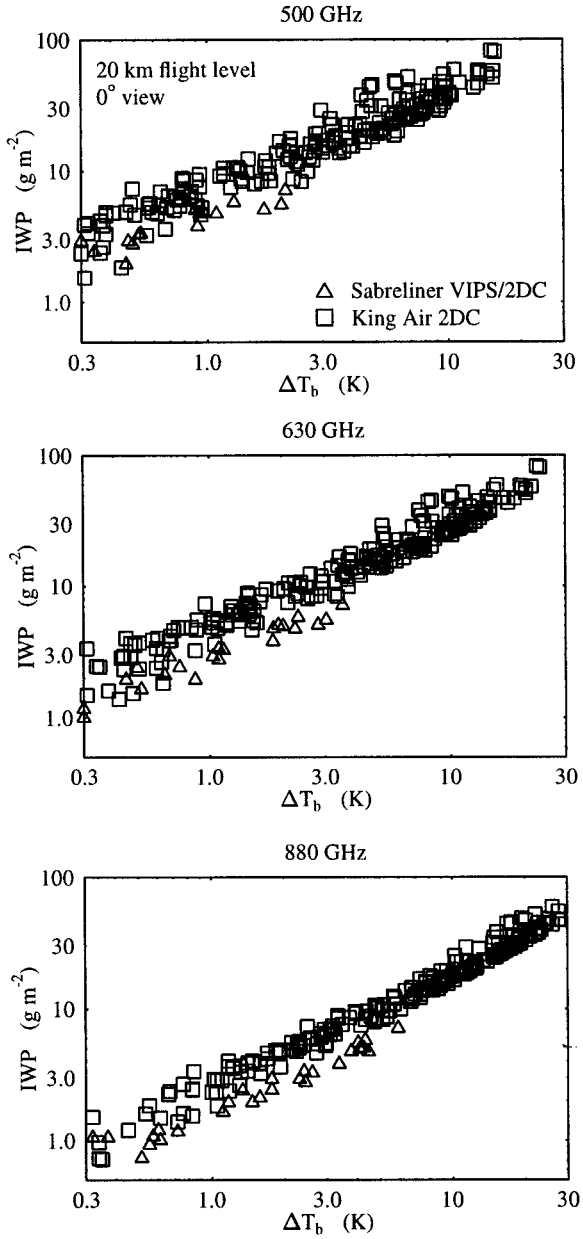

FIG. 5. Scatterplots of ice water path (IWP) vs brightness temperature difference (ΔT_b) for 500, 630, and 880 GHz for ice cloud size distributions measured during FIRE II.

To summarize these results, regressions (log–log) are performed for IWP as a function of ΔT_b. Table 5 lists the regression results for the King Air distributions having $\Delta T_b > 0.3$ K for 150, 200, and 340 GHz, and $\Delta T_b > 1.0$ K for 500, 630, and 880 GHz. The IWP corresponding to $\Delta T_b = 1$ K (coefficient a) decreases with increasing frequency. The slope b also increases with frequency as ΔT_b becomes less sensitive to particle size. The rms fractional error decreases with increasing frequency. The errors at higher frequencies (20%–30%) are due to the relatively good correlation of IWP and particle size in the King Air dataset and does not treat uncertainties due to varying particle shape. These types of regression relations suggest a simple retrieval algorithm that could be used for a single-frequency submillimeter radiometer. In this case, the variation of particle size as well as particle shape would be sources of error. The problem with this approach is that the regression coefficients depend on the characteristics of the microphysical dataset employed and would not be generally applicable. In particular, these FIRE King Air distributions are not representative of all cirrus clouds because they are biased toward high IWP and large particles.

TABLE 5. Fit parameters for ice water path as a function of brightness temperature difference [IWP = $\alpha(\Delta T_b)^b$, with ΔT_b in degrees kelvin and IWP in grams per square meter] for six frequencies and three viewing angles/polarizations. The rms error in ln(IWP) is also listed. These relations are for FIRE II King Air distributions modeled in a midlatitude summer atmosphere for nadir (downward) viewing.

Frequency	View	a	b	Std error
150	0	48.65	0.455	0.330
150	49V	48.56	0.531	0.306
150	49H	40.85	0.476	0.332
220	0	25.86	0.446	0.346
220	49V	24.28	0.560	0.307
220	49H	20.39	0.515	0.362
340	0	11.60	0.560	0.382
340	49V	10.57	0.643	0.304
340	49H	8.69	0.585	0.387
500	0	6.13	0.684	0.330
500	49V	5.72	0.692	0.274
500	49H	4.43	0.661	0.347
630	0	3.83	0.794	0.286
630	49V	3.57	0.757	0.250
630	49H	2.63	0.749	0.323
880	0	1.96	0.917	0.225
880	49V	1.64	0.868	0.207
880	49H	1.14	0.894	0.274

4. Modeling results

a. Sensitivity properties

The basic results of the millimeter-wave and submillimeter-wave radiative transfer modeling for various cirrus cloud properties can be described in terms of the sensitivity. The radiometric signal produced by a cirrus cloud is the change in brightness temperature (ΔT_b) between a cloudy and cloud-free sky assuming identical atmospheric gas and temperature profiles. The ''sensitivity'' is defined as ΔT_b normalized by IWP along the viewing direction $S = |\Delta T_b|$/IWP. The value of S is constant in the linear regime of radiative transfer. As a rule of thumb, the radiative transfer is linear (to within 10%) with IWP for $\Delta T_b < 30$ K, above which the sensitivity falls significantly. In this section, the ice clouds are modeled by gamma distributions specified by the IWP, the median equivalent mass sphere diameter $D_{\rm me}$, and the width parameter α. The modeled cirrus cloud

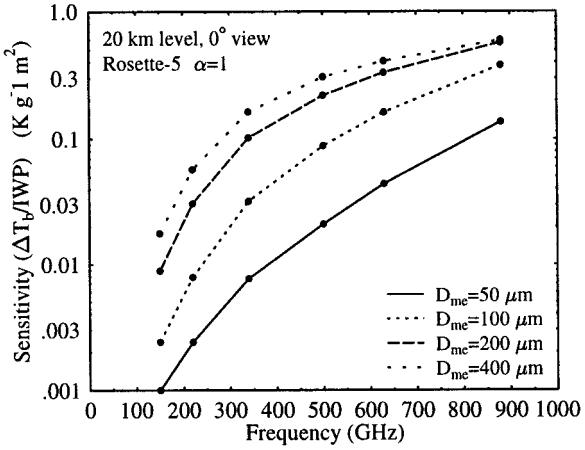

FIG. 6. Sensitivity (ratio of ΔT_b to ice water path) as a function of frequency for four gamma size distributions of five-bullet rosette crystal shape. A nadir-viewing geometry is assumed.

top is at the tropopause in a standard midlatitude summer atmosphere.

Figure 6 illustrates the value of submillimeter frequencies for cirrus remote sensing. For characteristic particle sizes typical of cirrus clouds, the sensitivity increases rapidly with frequency, and only frequencies above 500 GHz have adequate sensitivity (greater than 0.1 K g^{-1} m^2) for cirrus. The sensitivity curves for the large D_{me} appear to approach a limit because the gamma distributions are truncated at a particle size of 1000 μm.

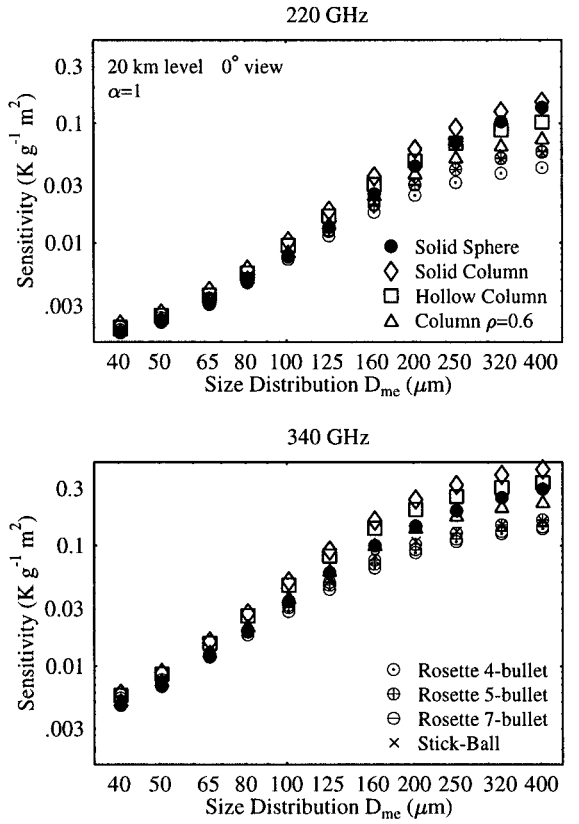

FIG. 7. Sensitivity (ΔT_b/IWP) at 220 and 340 GHz as a function of distribution particle size for eight particle shapes.

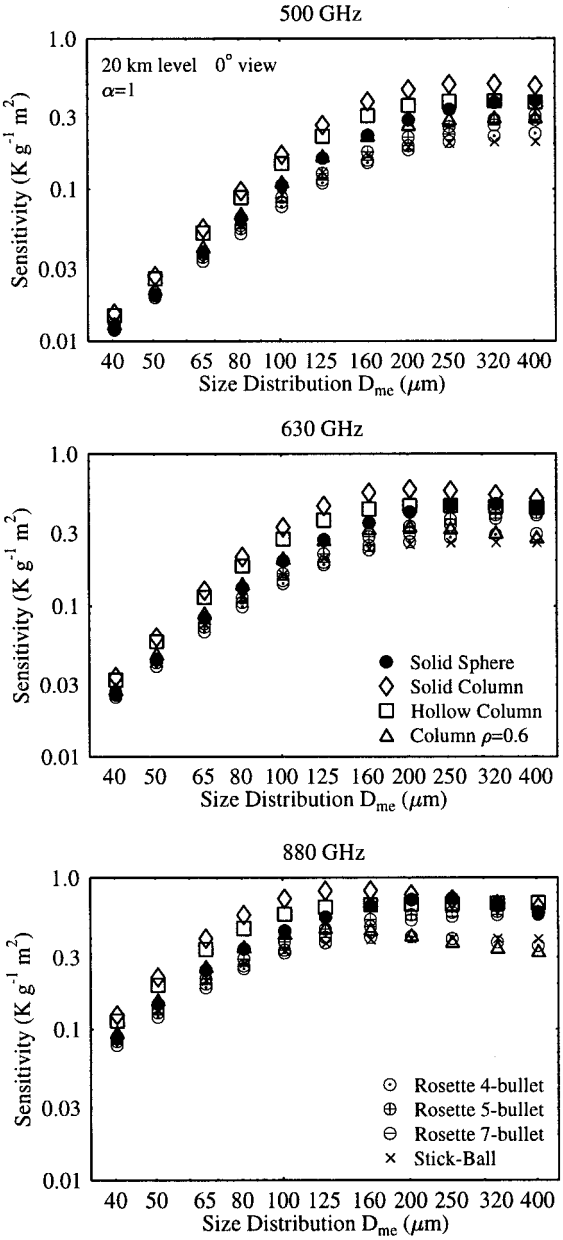

FIG. 8. Sensitivity (ΔT_b/IWP) at 500, 630, and 880 GHz for nadir viewing as a function of distribution particle size for eight particle shapes.

The effect of particle size on nadir sensitivity may be seen in Figs. 7 and 8. For low frequencies the sensitivity increases continuously with particle size, but for higher frequencies the sensitivity increases for smaller particles sizes and then levels off as the particle size approaches the wavelength. The constant sensitivity is highly desirable because it implies that the ΔT_b signal

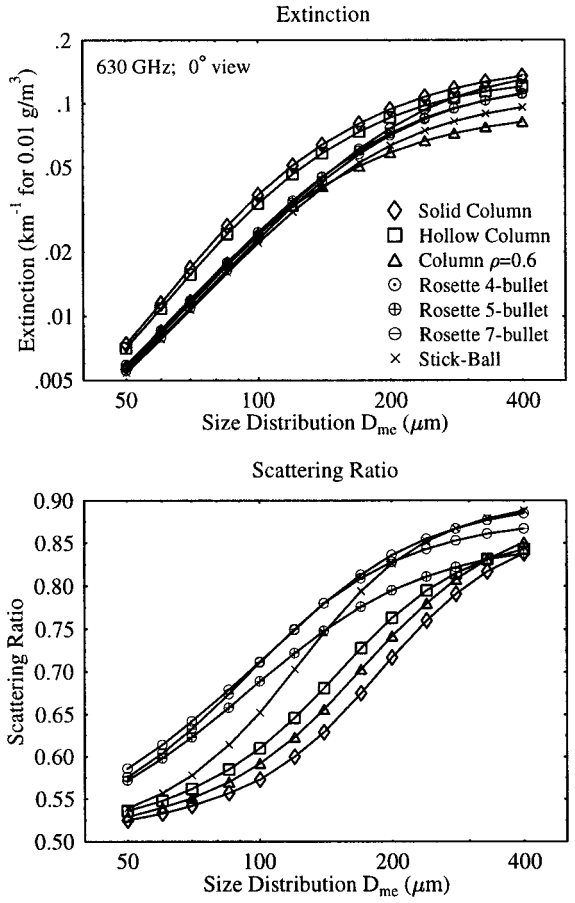

FIG. 9. Extinction and forward scattering ratio at 630 GHz for a nadir view angle for seven shapes.

is proportional to cloud IWP. The particle size at which the sensitivity levels off decreases with increasing frequency, so that for 880 GHz the sensitivity is relatively independent of particle size for $D_{me} > 100$ μm. Using a threshold of $\Delta T_b > 2$ K at 880 GHz, IWP could be detected down to 5 g m^{-2} for size distributions with $D_{me} > 125$ μm. The higher frequencies not only provide a greater sensitivity to cirrus but also a reduced dependence of IWP on particle size.

The effect of particle shape is evident in Figs. 7 and 8. For the smaller sizes and lower frequencies, the ice particles are in an absorbing regime (low single-scattering albedo). Since the absorption is proportional to volume, there is little variation in sensitivity with shape. With increasing size parameter, particle shape becomes more important. The maximum range in nadir sensitivity due to particle shape is a factor of 3.6, 3.2, 2.6, 2.4, and 2.3, for 220, 340, 500, 630, and 880 GHz, respectively. For the most part, the sensitivity of columns is well above that of the rosettes. This may be understood from the single-scattering properties. Figure 9 shows the extinction and forward-scattering ratio for seven shapes as a function of D_{me}. High-density columns have both a higher extinction and a lower forward-scattering ratio as compared to rosettes or other lower-density shapes. Both of these characteristics increase the brightness temperature difference (consider the first-order radiative transfer results in the appendix). Based on in situ microphysical observations, it is likely that a prevalence of large columns is quite rare in cirrus clouds (Heymsfield and Platt 1984). How shapes change the relative sensitivities with D_{me} indicates that the radiative properties are not simply a function of particle size and bulk density but are affected by gross morphological features.

The sensitivity for horizontal and vertical polarization using a 49° downward-looking view angle is shown in Fig. 10. The 49V sensitivity tends to be below that at nadir, while the 49H sensitivity tends to be above. There is a substantial polarization effect due to a larger horizontal compared to vertical cross section for the oriented particles. The range in sensitivity due to shape is less for vertical than for horizontal polarization. Excluding spheres as unrealistic, the maximum range of sensitivity at 630 GHz is 1.7 for vertical and 2.3 for horizontal polarization. The range of vertically polarized sensitivity caused by varying particle shape, excluding spheres, continues to decrease with viewing angle out to $\cos\theta = 0.1$ viewing angle. The spherical particle shape, which is a reasonable approximation to the average sensitivity for nadir viewing, substantially overestimates the vertical polarization sensitivity at oblique angles ($\cos\theta < 0.5$).

The sensitivity is not greatly affected by the width of the gamma size distribution (as measured by α). The wider distributions cause less change in sensitivity with D_{me} than do the narrower distributions. For nadir viewing of rosettes at 630 GHz, the ratio of sensitivity for $\alpha = 7$ (narrow) to that for $\alpha = 0$ (wide) goes from 0.71 at $D_{me} = 40$ μm to 1.09 at $D_{me} = 400$ μm. The effect of the size distribution width on the sensitivity tends to be smaller than the effect due to particle shape.

In absolute value, the brightness temperature change due to cirrus for upward- and downward-viewing geometry is nearly the same except for the smaller size distributions. For nadir viewing of rosettes at 500 GHz the upward-viewing sensitivity from 10 km is within 15% of that for downward viewing from 20 km for $D_{me} \geq 125$ μm (increasing to 80% higher for $D_{me} = 50$ μm). This is expected from the first-order radiative transfer model (see the appendix). The larger size distributions have a single-scattering albedo near unity (mainly scattering) and so the upwelling and downwelling sensitivities are very close. The smaller size distributions are more absorbing, and so the radiation that is emitted reduces the brightness temperature decrease for upwelling radiation but augments the brightness temperature increase for downwelling radiation.

b. Observable signatures of particle size and shape

Sensitivity is primarily dependent on particle size, and thus accurate retrieval of IWP requires knowledge

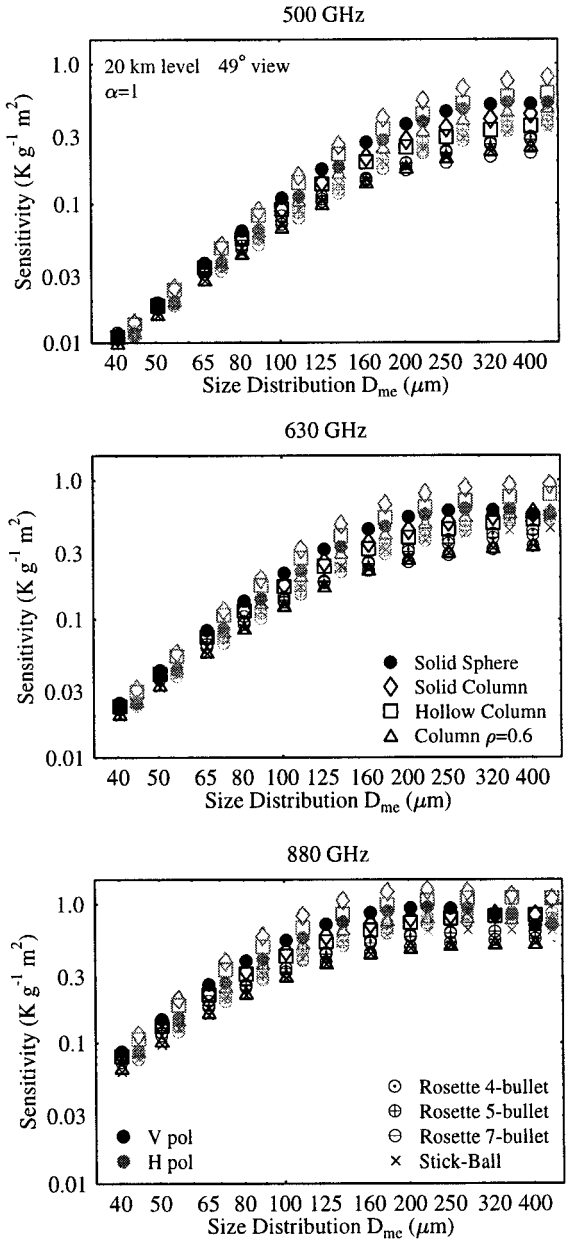

FIG. 10. Sensitivity at 500, 630, and 880 GHz for a 49° downward-viewing angle as a function of distribution particle size for eight particle shapes. The horizontal polarization sensitivity is in gray and has been offset from the vertical polarization results.

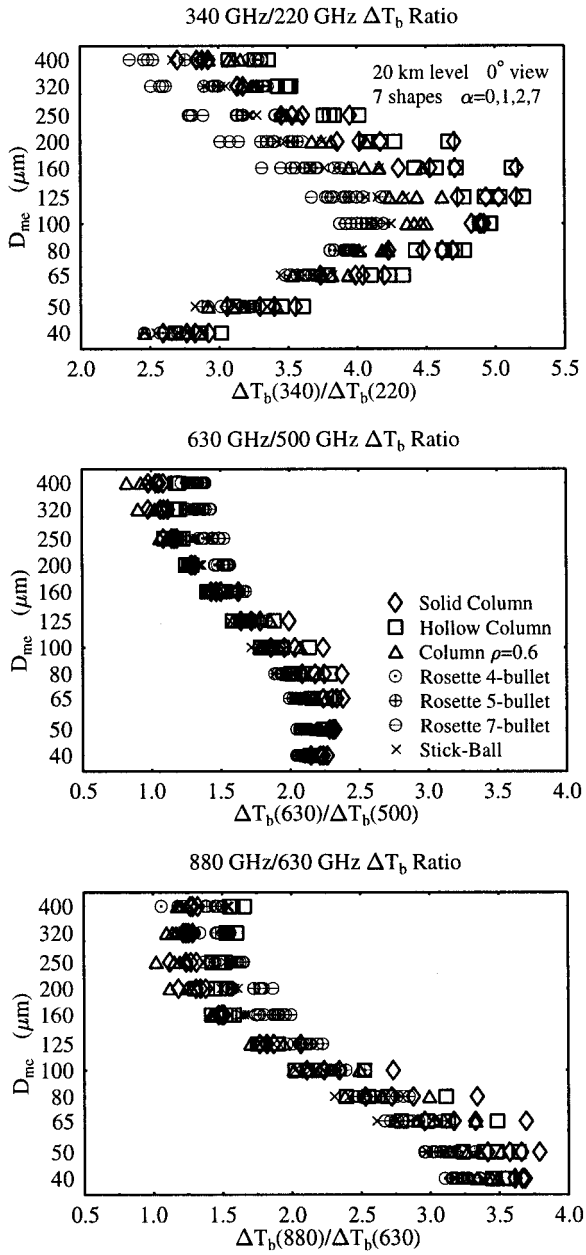

FIG. 11. The dependence of particle size (D_{me}) on the ratio of brightness temperature depression (ΔT_b) at two frequencies. Four size distribution widths (α) and seven particle shapes are modeled.

of particle size. As discussed in Evans and Stephens (1995b), the ΔT_b's at two different microwave frequencies contain information about particle size. Figure 11 shows the size distribution parameter D_{me} as a function of the ratio of the ΔT_b's. The ratio of ΔT_b at 340 GHz to ΔT_b at 220 GHz does not uniquely determine particle size and is only useful for $D_{me} > 200$ μm. The ratios of ΔT_b at 630 and 500 GHz are smaller because these two frequencies are relatively close. The 630–500-GHz pair does not distinguish the smaller particle sizes ($D_{me} > 100$ μm) very well. The ratio of ΔT_b at 880 and 630 GHz can be used to determine the median particle size over a wider range of sizes ($\sim 65 \leq D_{me} \leq \sim 200$ μm). For larger particles, the ability to discriminate particle size with the 880–630-GHz pair is limited. In this regime, however, the sensitivity is independent of size, so that the determination of IWP is minimally affected.

The polarization signature and its relation to particle shape is shown in Fig. 12. The abscissa is the dual-frequency axis indicating particle size and the ordinate is the polarization axis. There is a rough sorting by shape

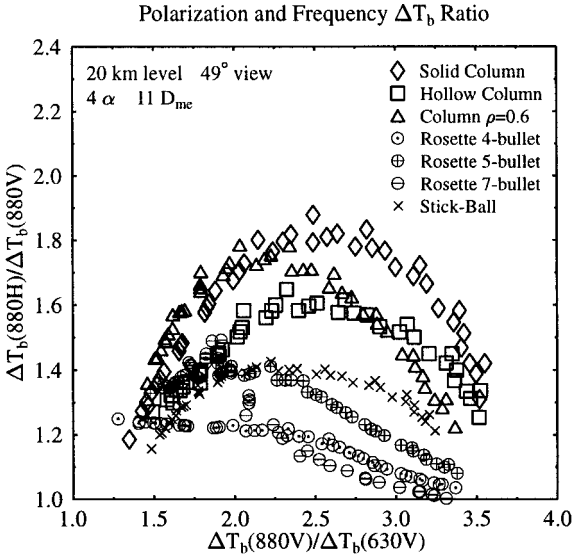

FIG. 12. Ratio of brightness temperature depression (ΔT_b) at the two polarizations vs the ratio of ΔT_b at two frequencies. The viewing geometry is downward at 49°. The seven particle shapes are indicated by symbols, and for each shape there are 44 cases of particle size (D_{me}) and distribution width (α).

with the columns having a larger polarizing signature than the rosettes or irregular shape. This is a result of columns having a horizontal orientation and a higher aspect ratio. At a viewing angle of 49° for 880 GHz, a polarization ratio of 1.4 could be used as a criterion for discriminating between rosettes and columns. The polarization signature at this frequency is useful for distinguishing between these shapes for particle sizes in the range $\sim 65 \leq D_{me} \leq \sim 200$ μm. Cirrus clouds have a variety of rosette shapes in various orientations, so that the observed polarization would be less than the modeled value. Actual cirrus clouds contain a mixture of shapes and so the polarization signature will be more difficult to interpret. However, polarization measurements should be pursued to further investigate their value in retrieving particle shape information.

5. Retrieval method and error analysis

a. Determining ΔT_b

The measured radiometric signal T_b is the sum of the ice cloud effect ΔT_b and the clear-sky ''background'' brightness temperature T_{b0}. Thus, the background T_{b0} must be inferred to derive the desired ΔT_b. In the simple case where no midtroposphere liquid clouds are present, the background brightness temperature is due to the water vapor emission. One way to obtain the background T_{b0} is to average nearby clear-sky pixels and assume continuity of the atmospheric profile. The error in this ''pixel differencing'' technique for ΔT_b depends on the local structure of the temperature and water vapor profiles. The variability in brightness temperature of the MIR 183.3 $\pm$ 1-GHz channel (which matches submillimeter water vapor absorption reasonably well) was analyzed in Deeter and Evans (1997). Autocorrelation analysis of more than 900 km of flight tracks containing cirrus clouds in the Tropics indicated the rms variability in T_b for a 30-km correlation length (i.e., distance between cirrus and clear-sky patch) was about 1.5 K. The variability is probably greater in more complex meteorological conditions, such as midlatitude frontal regions. Supercooled liquid water clouds, which would be high enough for a submillimeter radiometer to detect above the water vapor screening, would also be a source of background variability. Their impact is potentially large for multilevel cloud situations, but this issue is left for future study.

A much more accurate technique for obtaining ΔT_b is to use a 183-GHz radiometer to predict the background submillimeter brightness temperature. A water vapor line is located at 183 GHz, which can be used to match the water vapor opacity at submillimeter frequencies. The 183-GHz frequency is also relatively insensitive to cirrus-induced scattering. For high IWP and large particles that can slightly affect the 183-GHz channel, the ΔT_b at 183 GHz from an ice cloud would be obtained iteratively in the retrieval process. Modeling is performed to estimate the ability of the 183-GHz channel to predict the clear-sky brightness temperature at 643 GHz, a frequency studied for space applications. Atmospheric profiles are generated by setting the relative humidity at each tropospheric level to a random value between 20% and 80%. The temperature is varied at each tropospheric level uniformly from the standard atmosphere by -2 to 2 K. For each of four standard profiles, 100 profiles are generated, and the 183-GHz and submillimeter brightness temperatures computed. The frequency offset from the 183-GHz line center was varied to find the best match in water vapor transmission profiles, which occurred at ± 1.6 GHz from line center. An integration over the radiometer bandwidths was included. Figure 13 shows the 643-GHz T_b versus the 183-GHz channel T_b for the four standard atmospheres. The shift between the warm and cold atmospheres is due to differences in the pressure dependence of the submillimeter windows (line wings) and the 183-GHz frequency (line center). Auxiliary information could be used to constrain the temperature profile. Therefore, the scatter about the linear regression calculated for each standard profile gives the accuracy of this technique. The rms uncertainty in the predicted submillimeter background T_{b0} is less than 0.25 K for each atmosphere.

b. Effects of atmospheric absorption

Because of water vapor opacity, a submillimeter radiometer is sensitive only to upper-tropospheric clouds, which are above the bulk of the water vapor. Figure 2 shows submillimeter transmission profiles in atmospheres of varying water vapor content. The reduced

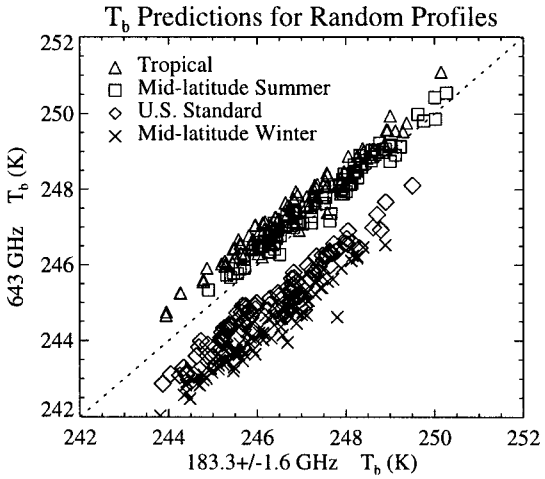

FIG. 13. Scatterplot showing how well the clear-sky brightness temperature at 643 GHz can be predicted from that at 183.3 ± 1.6 GHz. Results for 200 random profile temperature and relative humidity perturbations in each of four standard atmospheres are shown.

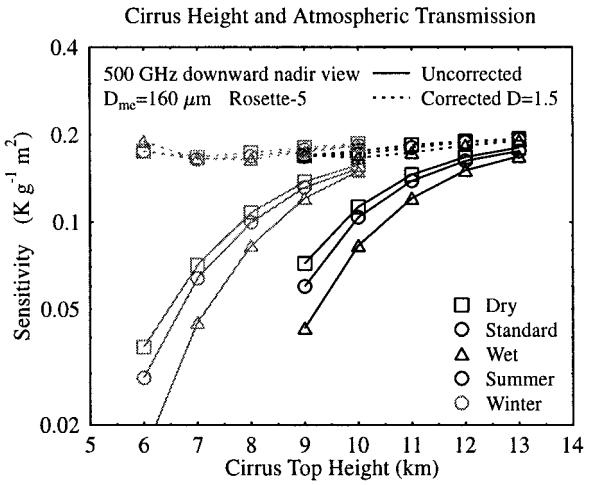

FIG. 14. Sensitivity at 500 GHz as a function of cirrus cloud top height for three summer and three winter atmospheres with different humidities. The cloud thickness is 1 km. The viewing geometry is downward looking from 20 km. Along the original sensitivities, the corrected sensitivities using atmospheric transmission and a diffusivity factor of 1.5 are shown. Dark solid lines represent summer profiles, grey lines represent winter profiles, and dashed lines show the corrected sensitivities (6) for each of the six cases.

transmission also decreases the sensitivity to lower, warmer ice clouds. Even in a completely saturated troposphere, the transmission at submillimeter window frequencies is greater than 0.8 down to about the −40°C level. In addition to the direct transmission effect, the sensitivity is also decreased due to backscattering of downwelling radiation incident on the cloud (as absorption increases above the cloud there is more emission incident on the cloud). These effects are understood best with the first-order radiative transfer model described in the appendix. It is shown that the sensitivity compared to having no absorption in and above the clouds is reduced by the factor $\mathcal{T}_o\mathcal{T}_a^D$, where $\mathcal{T}_o$ is the transmission from the cloud to the observer, $\mathcal{T}_a$ is the nadir transmission above the cloud, and D is the diffusivity factor (e.g., $D = 1.5$). Besides the water vapor transmission effect, the atmosphere affects the sensitivity because ΔT_b is proportional to the upwelling radiance. These two effects may be combined to define a corrected sensitivity S,

$$S = S_{\text{obs}} \frac{250\ \text{K}}{I\uparrow_{\text{clr}}} \frac{1}{\mathcal{T}_o^{1/\mu}\mathcal{T}_a^D}, \tag{6}$$

where S_{obs} is the original sensitivity and $I\uparrow_{\text{clr}}$ is the upwelling clear-sky brightness temperature. An illustration of how the sensitivity is reduced as the cirrus height decreases is shown in Fig. 14. As the cloud height is lowered, the sensitivity is reduced substantially, though the correction method (6) works quite well for a nadir transmission above 0.5.

The accuracy of the correction procedure for cirrus height is quantified by calculating the spread in sensitivity. The maximum range in sensitivity is computed separately for the three relative humidity profiles, over nine size distributions, two particle shapes, and five cirrus levels. A correction is attempted only when the nadir transmission to the cloud is greater than 0.5. The range in sensitivity at 500 GHz is listed in Table 6. The success of the sensitivity correction shows that the atmospheric transmission effect is well understood.

With a measurement of upper-tropospheric water vapor (i.e., from 183-GHz water vapor line measurements or from infrared water vapor channels above the cloud) and the height of the cirrus cloud (from radar, lidar, thermal IR estimate, etc.), the submillimeter water vapor transmission could be estimated and the correction applied. On the other hand, the sensitivity variation with transmission can be used to define what the upper-tropospheric ice clouds are. The transmission curve prevents a space-based submillimeter radiometer from seeing mid- and lower-troposphere clouds. The ''filter'' selecting the observation altitudes is the atmospheric transmission to about the 2.5 power. This filter depends primarily on temperature (assuming average relative humidities) and can be applied to climate model simulations to define ''upper-tropospheric ice mass.''

TABLE 6. Range in sensitivity at 500 GHz for two viewing angles (nadir and 49°) and two atmospheres [midlatitude summer (MLS) and midlatitude winter (MLW)]. The range for uncorrected (UnC) and corrected (Cor) sensitivities is expressed as a ratio. Diffusivity factors are $D = 1.5$ for the 0° view and $D = 2.0$ for the 49° view.

	0° view		49°V view	
Atmosphere	UnC	Cor	UnC	Cor
MLS	4.07	1.20	7.19	1.25
MLW	5.56	1.16	10.37	1.36

c. A two-channel retrieval algorithm

Ice water path and particle size are the primary determinants of submillimeter ΔT_b. Figure 11 showed that two separate frequencies may be used to separate particle size from IWP. A simple two-channel algorithm (Evans et al. 1996) was developed that used the ratio of ΔT_b at two frequencies to predict the sensitivity with a regression relation. Since the IWP was determined from the sensitivity, this required linearity in the radiative transfer. Here, a more sophisticated Bayesian algorithm is used to retrieve the IWP and size distribution $D_{\rm me}$ from measurements at two frequencies. The effects of size distribution width α, particle shape, and radiometer noise/background error are considered as error sources.

The 11 values of $D_{\rm me}$ and 16 values of IWP used for the radiative transfer simulations form a retrieval grid. The simplest way to use this grid would be to find the IWP–$D_{\rm me}$ pair that minimizes the difference between the observed and simulated ΔT_b. This approach performs poorly, however, because the correlation between the two channels causes the retrieval to be ill conditioned. Thus, as with many remote sensing algorithms that use first guesses or statistical methods, a priori information must be added. The following Bayesian algorithm supplies a priori information about particle size. Unless there is strong reason to believe from the observations that the particle size is small, it is safer to assume a larger particle size where the sensitivity–particle size relation is flat. The prior distribution thus prevents errors in ΔT_b from biasing the solution toward smaller particle size and larger IWP.

The addition of extra information is done formally with the Bayes theorem (Larson 1982). The posterior probability distribution $P_{\rm post}$ is related to the prior probability distribution $P_{\rm prior}$ and the conditional distribution $P_{\rm cond}$ by

$$P_{\rm post}({\rm IWP}, D_{\rm me} \,|\, \Delta T_1, \Delta T_2) \propto P_{\rm prior}({\rm IWP}, D_{\rm me})\, P_{\rm cond}(\Delta T_1, \Delta T_2 \,|\, {\rm IWP}, D_{\rm me}). \quad (7)$$

The conditional distribution represents the forward radiative transfer problem (ΔT_b given the cirrus properties) and is assumed to be of bivariate normal form. The distribution mean and covariance parameters for each IWP–$D_{\rm me}$ grid point are obtained from the ΔT_b simulated for the particle shapes and size distribution widths combined with an assumed level of uncorrelated Gaussian noise. The prior distribution is assumed to be a lognormal distribution in $D_{\rm me}$, specified by a geometric mean and standard deviation of the log chosen subjectively.

The IWP retrieval is done in a two-step process (see Fig. 15). First, the geometric mean relation between the ΔT_b at the higher frequency and corresponding IWP is found for each $D_{\rm me}$ grid value. Thus, for a given observation (ΔT_2), the IWP corresponding to each grid $D_{\rm me}$ is found. The required particle size information

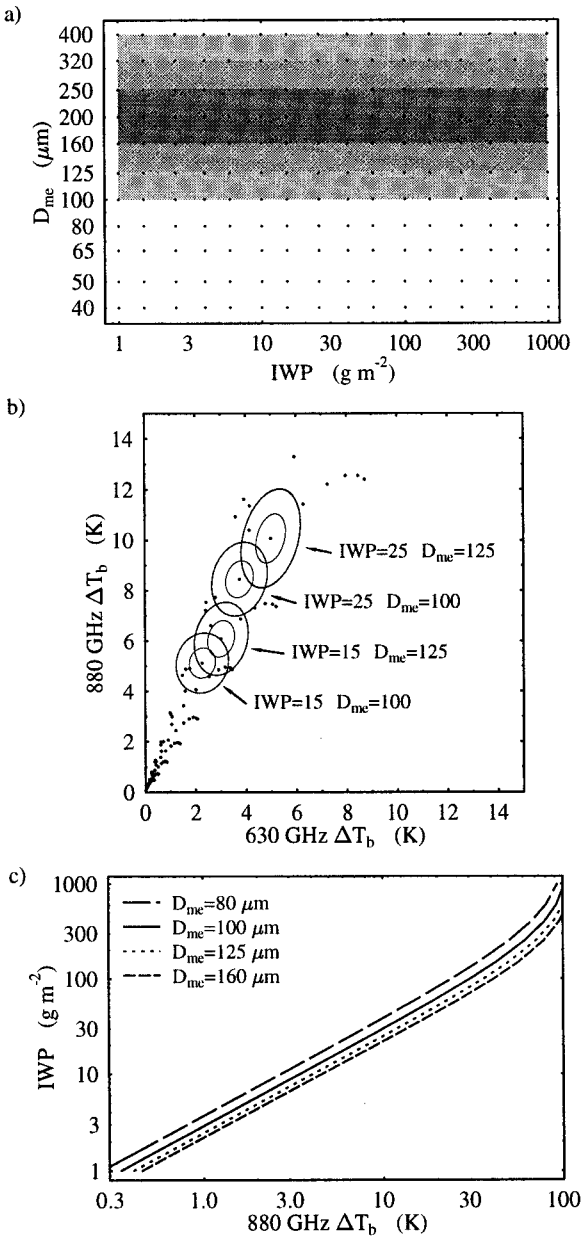

FIG. 15. A schematic diagram of the Bayesian submillimeter ice cloud retrieval algorithm using actual values for 630/880-GHz nadir viewing. (a) The retrieval grid of 16 ice water paths (IWPs) and 11 particle sizes ($D_{\rm me}$'s) with the lognormal prior probability density function of $D_{\rm me}$ depicted with shading (for mode of 200 μm and standard deviation of 1 dB).(b) The mean values of the two observable ΔT_b corresponding to the IWP/$D_{\rm me}$ grid. The Gaussian probability densities for four grid points are depicted with one and two sigma ellipses. The variances and correlations between the two ΔT_b's for a single IWP/$D_{\rm me}$ point are caused by 28 modeled cases of particle shape and size distribution width and by the addition of 0.5-K uncorrelated noise in each channel. These Gaussian pdf's represent the Bayesian conditional probability distribution and are used to find the mean $D_{\rm me}$ by summing over all IWP/$D_{\rm me}$ grid points for the observed ΔT_b's.(c) Relations depending on particle size $D_{\rm me}$ between ice water path and the high-frequency ΔT_b. The ΔT_b determines an IWP for each grid $D_{\rm me}$, and these are then weighted by the Bayesian posterior distribution of $D_{\rm me}$. This is akin to using the Bayesian posterior mean particle size to select the appropriate IWP–ΔT_b relation.

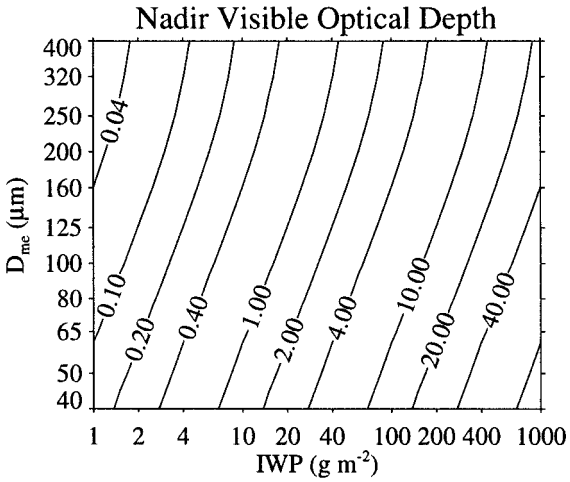

FIG. 16. Visible optical depth for nadir viewing for the modeled range of ice water path and particle size (D_{me}). The optical depth is computed from the particle area. The slight curve in the contours for large D_{me} is due to the gamma distribution truncation.

comes from the Bayes posterior probability. The retrieved IWP is computed by weighting IWP (D_{me}) by the posterior probability and summing over all the retrieval grid points. The retrieved D_{me} is found more directly by computing the mean D_{me} over the grid using the posterior probability. However, so as to not bias the D_{me} retrieval, the prior distribution is taken to be uniform. The best choice of D_{me} prior distribution parameters depends on the frequency pair and observation angle being considered.

d. Retrieval error analysis

The algorithm described in the last section is used to perform an error analysis, primarily on IWP, using a Monte Carlo procedure. This involves adding noise to the modeled ΔT_b's and then using the two-channel retrieval algorithm to invert for IWP and D_{me}. The error is estimated with a comparison of the retrieved IWP and D_{me} with the input values. For each of the 11 discrete D_{me} and 16 IWPs the Monte Carlo procedure is performed with 15 realizations of Gaussian noise added to the simulated ΔT_b for seven particle shapes (excluding spheres) and four size distribution α's. The noise at each frequency is assumed to be uncorrelated and has an rms of 0.5 K, which is a realistic estimate of the minimum measurement noise. Retrievals are not made for realizations with ''observed'' ΔT_b below two standard deviations above the rms noise level (0.5 K). The retrieved values are compared to the true values in a relative sense by computing the rms difference in the logarithms of the values. This is then exponentiated to obtain the error factor. Thus, an rms error factor of 1 indicates no error, while an error factor of 2 means an rms range from -50% to $+100\%$. For small rms error factors, a factor of 1 may be subtracted to obtain the one standard deviation fractional error (e.g., a factor of 1.3 implies about 30% error).

The visible optical depth corresponding to the range of IWP and D_{me} is shown in Fig. 16. To visualize how the accuracy varies with ice cloud properties, the rms error factor is displayed as contour plots of IWP and D_{me}. Regions beyond an error factor of 2, or where the noise threshold is not reached for half of the cases, are not contoured. The IWP error analysis is shown for three frequency pairs (220/340, 500/630, and 630/880) in Fig. 17. The 220/340-GHz pair yields the worst performance and is insensitive to most cirrus. The accuracy and range of utility improve for the higher frequencies. The 630/880 retrieval accuracy achieves an error factor of 1.4 or below for IWP above 5 g m^{-2} and D_{me} above 100 μm. Where there is sufficient signal to noise, the majority of the error is caused by uncertainty in particle shape. Since columns have significantly higher sensitivity than the rest of the shapes and are rare in cirrus clouds, it is interesting to consider the IWP retrieval errors without columns (Fig. 18). The rms errors for 630/880 GHz are below 30% for IWP $>$ 10 g m^{-2} and $D_{me} > 100$ μm and are below 20% for higher IWP.

Since cirrus clouds are layer clouds with horizontal dimensions typically 100 km or more, oblique viewing angles ($0.1 < \cos\theta < 0.3$) offer a simple way to increase the radiometer sensitivity to a given amount of vertically integrated IWP. The radiometer field of view (footprint) expands for oblique viewing angles, but the linear nature of submillimeter radiometry still integrates over cloud inhomogeneities to provide the total ice mass. Figure 19 shows the rms error factor for IWP and D_{me} at $\cos\theta = 0.3$ ($\theta = 73°$) viewing angle. Using the horizontal polarization at 630/880 GHz further improves the sensitivity. For this oblique angle, the IWP errors are worse for small particle sizes, but the 1.4 rms error factor contour now goes down to IWP = 1 g m^{-2} (or visible optical depth below 0.1).

This error analysis is inherently dependent on the modeling assumption. The baseline cases may be conservative since a wide range of α (0–7) is used, and actual particle shapes may not have as great a range of submillimeter scattering properties as the seven considered here. It is difficult to accurately quantify the error due to particle shape until more is known about cirrus particle shapes globally. While the 183-GHz technique for determining the ΔT_b from the observed brightness temperature is highly accurate for water vapor and temperature variations, supercooled water clouds will increase the error in some multilayer cloud situations. The effect of water vapor absorption on sensitivity is not included in this error analysis and perhaps is best thought of as a filter reducing the sensitivity to lower ice clouds.

e. A combined millimeter radar–submillimeter radiometer method

Recently, aircraft-based millimeter-wave radars, such as the NASA 94-GHz Airborne Cloud Radar developed

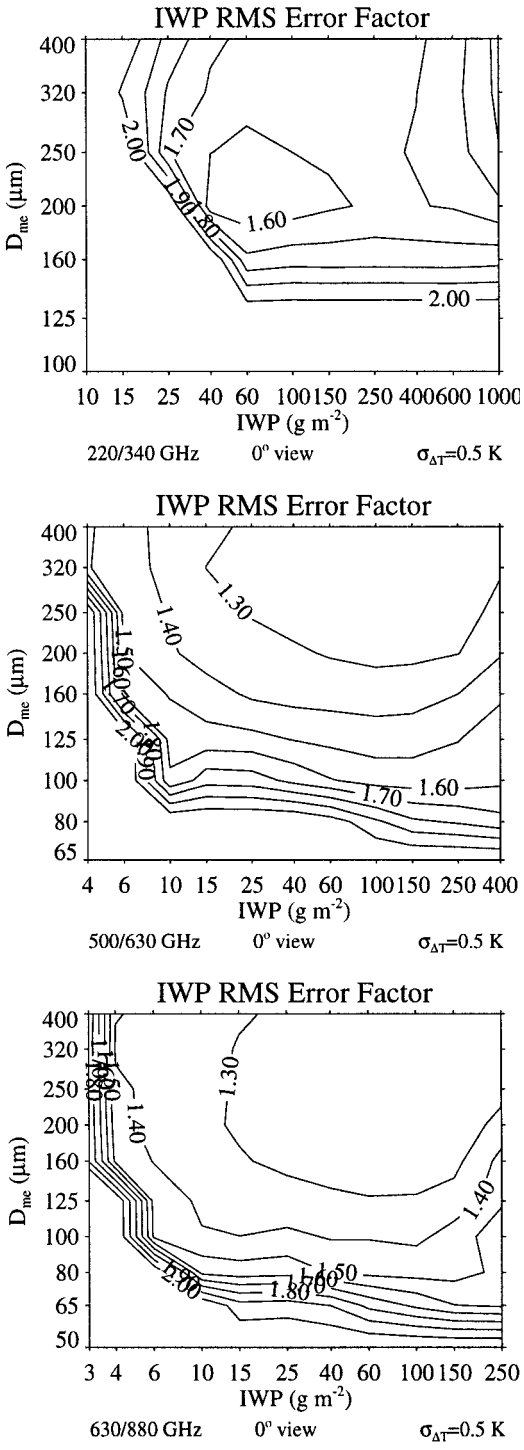

FIG. 17. The rms error factor for ice water path for ice cloud retrievals for three pairs of measurement frequencies using a nadir view. An error factor of 1 represents no error, and 2 implies a factor of 2 error. Uncorrelated Gaussian noise of 0.5-K rms is added to each channel. The D_{me} prior distribution parameters are a mean of 250 μm and std dev of 1.0 dB for 220/340 GHz, 200 μm and 1.5 dB for 500/630 GHz, and 200 μm and 1.0 dB for 630/880 GHz.

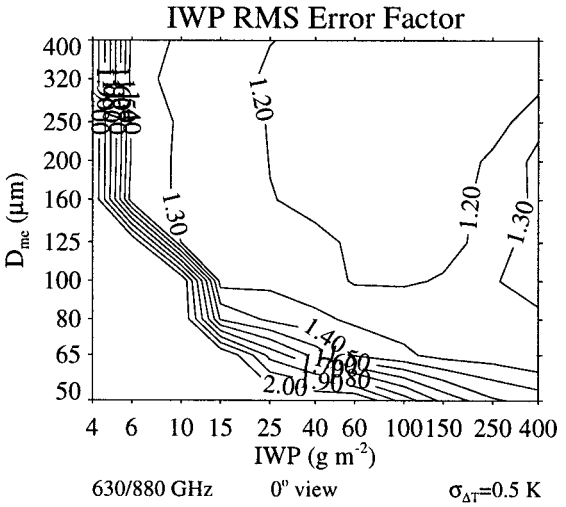

FIG. 18. The rms error factor for ice water path for ice cloud retrievals excluding the three column shapes for 630/880 GHz and nadir viewing. An error factor of 1 implies no error. The D_{me} prior distribution parameters are a mean of 200 μm and std dev of 2.0 dB.

jointly by JPL and the University of Massachusetts, have been shown to be a powerful new method for sensing cirrus cloud profiles. Radars measure cirrus-sized particles by Rayleigh scattering, and thus sense the sixth moment of the size distribution. Additional constraints on particle size are required to infer cloud ice mass with a radar. A submillimeter radiometer can provide the requisite particle size information.

The 94-GHz nadir radar reflectivity is simulated using the DDA technique for the same ice particle shapes and gamma size distributions used in the radiometer analysis. Since submillimeter radiometry measures a vertical integral of cirrus properties, the vertically integrated reflectivity (IZ) is the appropriate observable. Figure 20 shows the vertically integrated reflectivity sensitivity as a function of particle size. Since the IWP depends on the third moment, the reflectivity sensitivity increases with the third power of the size distribution D_{me}. The deviation from the D_{me}^3 line for large particles is primarily due to the gamma distribution truncation at the 1-mm particle size. The range in reflectivity sensitivity (factor of 2.1 at D_{me} = 100 μm) is mainly caused by the size distribution width α rather than particle shape, as is the case for submillimeter radiometry. The bottom panel in Fig. 20 illustrates that the differing dependence on particle size between radar and submillimeter radiometry may be used to infer D_{me} using the ratio of the two observables. Due to the decrease in 630-GHz sensitivity for smaller particles, the combined technique is less able to distinguish the smaller particle sizes.

The same Bayesian algorithm employed above is used to perform a Monte Carlo error analysis of a combined radar–radiometer algorithm. The submillimeter radiometer noise is assumed to dominate the radar noise (the radar usually would be far more sensitive). It proved

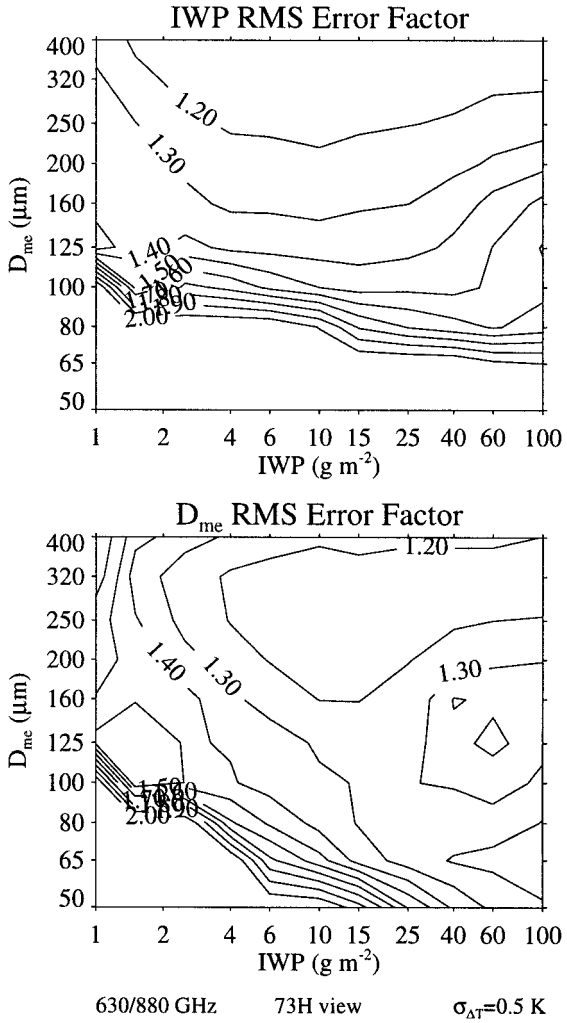

FIG. 19. The rms error factor for ice water path and particle size (D_{me}) for ice cloud retrievals for 630/880 GHz and 73° viewing angle with horizontal polarization. An error factor of 1 implies no error. The D_{me} prior distribution parameters are a mean of 200 μm and std dev of 1.5 dB.

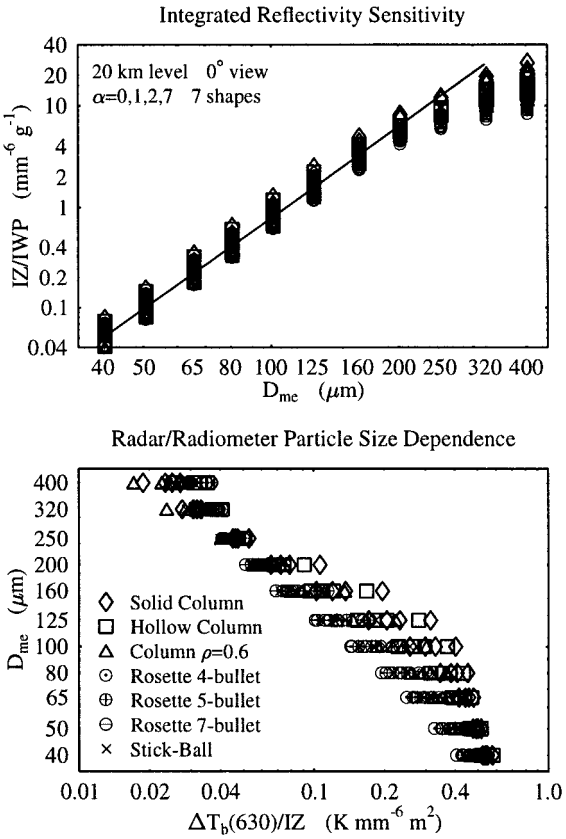

FIG. 20. Top: Integrated radar reflectivity sensitivity (IZ/IWP) as a function of distribution particle size (D_{me}) for seven particle shapes and four distribution widths (α). The D_{me}^3 line is also shown. Bottom: The dependence of particle size on the ratio of the 630-GHz radiometer ΔT_b to the integrated reflectivity (IZ).

more accurate to use the radiometer ΔT_b–IWP relationship rather than the radar IZ–IWP relationship. The rms error factors for IWP and D_{me} for the 94-GHz radar/630-GHz radiometer combination is shown in Fig. 21. The strongly differing dependence on particle size leads to rms errors of only 10%–30% in particle size. The IWP error is larger than for a purely submillimeter radiometer technique because only a single submillimeter radiometer frequency is used. Figure 21c shows that much of the IWP error is due to particle shape, and excluding the columns reduces the error to under 30% for IWP $>$ 10 g m^{-2} and $D_{me} > 100$ μm.

6. Summary and conclusions

The submillimeter radiometry technique for remote sensing cirrus clouds is explored with theoretical modeling. The scattering properties for eight particle shapes ranging from 10 μm to 1000 μm are modeled with the discrete dipole approximation. The brightness temperature change from clear sky (ΔT_b) due to cirrus clouds is simulated at 150, 220, 340, 500, 630, and 880 GHz with a polarized radiative transfer model. Observed ice cloud particle size distributions from FIRE II are modeled, and it is demonstrated that gamma size distributions are radiometrically equivalent if fitted with moments of the equivalent diameter (e.g., second and sixth).

The effect of various cirrus properties is quantified with the *sensitivity*, which is the ratio ΔT_b/IWP, where IWP is the cirrus ice water path. Cirrus properties are modeled with gamma size distributions specified by the median mass equivalent sphere diameter D_{me}. The sensitivity increases dramatically with frequency, so that at 880 GHz for nadir view, an IWP of only 5 g m^{-2} produces an easily measurable change in brightness temperature of $\Delta T_b > 2$ K for size distributions with $D_{me} > 125$ μm. For submillimeter frequencies, the sensitivity increases with crystal size for small particles but then levels off, which indicates that the ΔT_b signal is

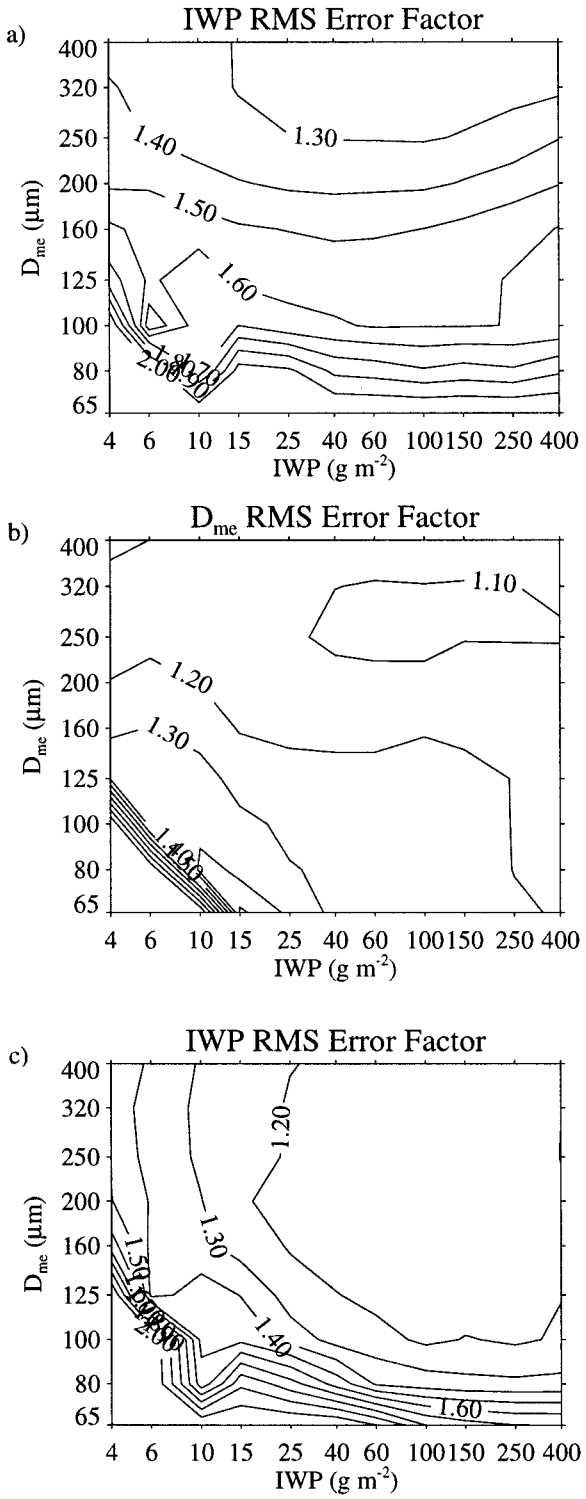

FIG. 21. The rms error factor for (a) ice water path, (b) particle size (D_{me}), and (c) ice water path for retrievals excluding the three column shapes. The retrievals simulations are for the 94-GHz radar/630-GHz radiometer combination with nadir viewing. An error factor of 1 implies no error. The D_{me} prior distribution parameters are a mean of 160 μm and std dev of 1.0 dB.

directly proportional to IWP. Column-shaped ice particles have higher sensitivity than rosettes. The brightness temperature increase for an upward-looking geometry is found to be about the same as the brightness temperature decrease for a downward-viewing geometry. The ratio of ΔT_b at two frequencies is a good measure of particle size over a substantial range. Atmospheric transmission is high enough in the submillimeter windows to allow upper-tropospheric sensing from both space and aircraft. Absorption by water vapor reduces the sensitivity to lower cirrus clouds; however, a method for ''correcting'' the sensitivity permits interpretation of clouds down to where the atmospheric transmission falls to 0.5.

The most promising method for obtaining the desired ΔT_b from the observed T_b is to derive the background ''clear-sky'' brightness temperature from a radiometric measurement at the 183-GHz water vapor line. This 183-GHz frequency is insensitive to cirrus and can match the water vapor transmission characteristics of the submillimeter channels. With this method the clear-sky T_b is predicted with an rms error of less than 0.25 K (even with large temperature and relative humidity variations). A two-channel retrieval algorithm for IWP and D_{me}, which uses the Bayes theorem to introduce a priori information about particle size, is described. This algorithm is used with a Monte Carlo error analysis to estimate the retrieval errors due to particle shape, size distribution width, and 0.5 K rms noise. The error analysis shows that the 220/340-GHz measurement pair is insensitive to most cirrus. The 630/880-GHz measurement pair for nadir viewing yields rms errors of 30% to 40% in IWP when IWP $>$ 5 g m^{-2} and $D_{me} > 100$ μm; there are similar errors for IWP $>$ 1 g m^{-2} and $D_{me} > 125$ μm for a viewing zenith angle of 73%. The same Bayesian algorithm is used to perform an error analysis on a combined 94-GHz radar/630-GHz radiometer technique. The combined method has rms errors of 10% to 30% for D_{me} and 30% to 60% for IWP. These error estimates depend on the modeling assumptions, which were chosen to be conservative.

The largest uncertainty in modeling submillimeter scattering by cirrus is the effect of particle shape. Although analyses of simulated radiances at orthogonal polarizations indicate that retrieving particle shape is difficult, it should be pursued further. In the future, in situ measured cirrus particle shape information could be used to develop shape retrieval techniques and more reliable estimates of the retrieval error. The real test of the submillimeter radiometric technique will be when observations are compared with properties obtained with in situ and other remote sensing methods.

This paper provides a theoretical basis for proposing characteristics for a dedicated radiometer for sensing cirrus clouds. It should have the following characteristics: 1) multiple frequencies for good sensitivity over a wide range of IWP and particle size, 2) a 183-GHz channel for determining the atmospheric emission back-

ground, 3) ability to scan to large viewing angles to achieve greater sensitivity, 4) minimum noise (i.e., below 0.5 K), and 5) dual polarization capability. The spacing of frequencies is a trade-off; a greater separation would result in a larger ratio of ΔT_b for determining particle size, but that also reduces the signal to noise at the lower measurement frequency. Based on matching the atmospheric transmission characteristics and constant ratios between the submillimeter channels, a radiometer with channels at 183, 495, 665, and 890 GHz is recommended. There are also atmospheric windows near 1350 and 1500 GHz that could be useful for sensing small cirrus particles, but these windows have significantly lower transmission. A radiometer dedicated to investigating clouds would include millimeter-wave and microwave channels for sensing tropospheric water vapor, liquid clouds, and precipitation. Finally, a submillimeter radiometer for sensing cirrus would be complemented by visible and infrared instruments to supplement the submillimeter retrievals with visible optical depth, cloud temperature, optically thin cirrus detection, and sizes of small particles.

Acknowledgments. The authors wish to thank Graeme Stephens for his support for this submillimeter radiometric technique (to the point of including it in a satellite mission proposal). Steve Aulenbach (funded by NASA FIRE-III Grant L55549D) helped prepare the FIRE microphysical datasets and provided valuable guidance in their use. Financial support to KFE and MND for this research was provided by NASA FIRE-III Grant NAG1-1702 and the JPL Director's Research and Development Fund. The work described in this paper was partially carried out by the Jet Propulsion Laboratory, California Institute of Technology, under a contract with the National Aeronautics and Space Administration. Financial support to SJW was provided by both the JPL Director's Research and Development Fund and NASA RTOP 460-4254.

APPENDIX

First-Order Radiative Transfer Model

A simple first-order scattering radiative transfer model is quite useful for understanding behavior of the radiance from different cirrus properties. The model presented here is a generalization of the one presented in previous work (Evans and Stephens 1995a). The assumptions of the model are that 1) the cloud is optically thin at submillimeter frequencies so the first-order scattering approximation may be made, 2) the incident radiation is unpolarized and hemispherically isotropic, and 3) there is no reflection from the rest of the atmosphere. Here, we allow gaseous absorption in and above the cloud so that there is incident radiation from above. Consider a cirrus layer with the incident radiance $I_b\uparrow$ at the bottom of the cloud and $I_t\downarrow$ at the top. The problem is to find the change in outgoing radiance due to the cirrus cloud at the bottom $\Delta I_b\downarrow$ and at the top $\Delta I_t\uparrow$. The cirrus cloud scattering properties are specified by the optical path τ, single scattering albedo ω, and the forward scattering ratio f. The gaseous absorption optical path within the cloud is τ_g. All of these properties and the outgoing radiances depend on the zenith angle (μ) and the polarization; the optical paths include the pathlength effect for the angle. For a particular upwelling, outgoing angle the forward scattering ratio is the ratio of the integral of the scattering matrix over upwelling incident angles to the integral over all angles. It is assumed that the cirrus properties are the same for upward and downward directions at the same angle. The Planck blackbody function at the frequency in question and the mean cloud temperature is $B_c = B_\nu(\overline{T}_c)$.

If the gaseous optical depth in the cloud layer is small, then the clear-sky outgoing radiance is

$$\text{Clear:}\quad I_t\uparrow = (1 - \tau_g)I_b\uparrow + \tau_g B_c$$

and

$$I_b\downarrow = (1 - \tau_g)I_t\downarrow + \tau_g B_c. \qquad \text{(A1)}$$

The outgoing radiance from the cirrus particles and gas is

$$\text{Cirrus:}\quad I_t\uparrow = (1 - \tau')I_b\uparrow + \tau'\omega' f I_b\uparrow + \tau'\omega'(1 - f)I_t\downarrow + \tau'(1 - \omega')B_c$$

and

$$I_b\downarrow = (1 - \tau')I_t\downarrow + \tau'\omega' f I_t\downarrow + \tau'\omega'(1 - f)I_b\uparrow + \tau'(1 - \omega')B_c, \qquad \text{(A2)}$$

where the total optical depth is $\tau' = \tau + \tau_g$ and the total single-scattering albedo is $\omega' = \omega\tau/\tau'$.

The difference between the radiance for cirrus cloud and clear-sky cases is

$$\Delta I_t\uparrow = \tau[-(1 - \omega f)I_b\uparrow + \omega(1 - f)I_t\downarrow + (1 - \omega)B_c]$$

and

$$\Delta I_b\downarrow = \tau[-(1 - \omega f)I_t\downarrow + \omega(1 - f)I_b\uparrow + (1 - \omega)B_c]. \qquad \text{(A3)}$$

Thus, for an optically thin cloud the procedure of subtracting the clear-sky signal from the cloudy signal eliminates the effect of the emission and attenuation by gases in the cloud.

At submillimeter frequencies the single-scattering albedo ω of the cirrus particles is near unity, except for the smaller sizes. For a cirrus cloud near the tropopause, the downwelling clear-sky radiance $I_t\downarrow$ is nearly zero. In this case, the radiance difference for upwelling radiation is negative, $\Delta I_t\uparrow \approx -\tau(1 - f)I_b\uparrow$, so there is a brightness temperature decrease. The radiance difference for downwelling radiation is positive, $\Delta I_b\downarrow \approx \tau(1 - f)I_b\uparrow$, so there is a brightness temperature increase

of the same magnitude. For smaller ice particles where the single-scattering albedo ω is not as close to 1, the brightness temperature increase for downwelling radiation will be somewhat larger than the upwelling brightness temperature decrease.

The water vapor transmission effect can be understood quantitatively using the first-order radiative transfer model. The model (A3) is for cirrus with the observer at the cloud boundary. At some distance away from the cloud, the intervening water vapor reduces the brightness temperature difference signal according to

$$\Delta I\uparrow_{\text{obs}} = \mathcal{T}_o(\mu)\Delta I_t\uparrow, \tag{A4}$$

where $\Delta I_{\text{obs}}\uparrow$ is the radiance difference at the observation point and $\mathcal{T}_o(\mu)$ is the transmission at the viewing angle μ between the cloud and the radiometer. Changing the atmospheric profile or cirrus height affects the cirrus Planck function B_c and the incident radiation $I_b\uparrow$ and $I_t\downarrow$. The effect of the emission of downwelling submillimeter radiation above the cirrus layer can be analyzed by comparing a lower cirrus layer case with the prototype case of the cirrus layer above all the water vapor absorption. The situation is simpler to analyze if the absorption by cirrus is ignored, and so $\omega = 1$, which is appropriate except for small ice particles.

For downward-looking geometries, the prototype signal is then

$$\text{Tropopause:} \qquad \Delta I\uparrow_{\text{proto}} = -\tau(1 - f)I\uparrow_{\text{clr}}, \tag{A5}$$

where $I\uparrow_{\text{clr}}$ is the clear-sky upwelling radiance. If the cirrus layer is moved down so that there is water vapor absorption/emission above it, then the downwelling incident radiation has to be considered. This downwelling incident radiation will be backscattered by the cirrus particles causing an increase in radiance, and hence reducing the magnitude of the cirrus sensitivity. The upwelling incident radiance will increase slightly, but this can be ignored. The resulting radiance difference signal is

$$\text{Lower:} \qquad \Delta I\uparrow_{\text{obs}} = \mathcal{T}_o(\mu)[-\tau_c(1 - f)I\uparrow_{\text{clr}} + \tau_c(1 - f)I_t\downarrow]. \tag{A6}$$

It is convenient to express the downwelling incident radiance in terms of the water vapor transmission above the cloud. Because of the greater path length, the downwelling incident radiance will be larger for slant paths at large angles. The appropriate incident radiance $I_t\downarrow$ in terms of the first-order radiative transfer model is some average over angles. This may be approximated with a diffusivity factor D, where $\overline{\mu} = 1/D$ is a characteristic mean cosine zenith angle. The mean downwelling incident radiance is then

$$I_t\downarrow = (1 - \mathcal{T}_a^D)B_a = (1 - e^{-D\tau_a})B_a, \tag{A7}$$

where $\mathcal{T}_a$ is the nadir transmission from space to the cirrus cloud due to water vapor absorption, and τ_a is the nadir optical depth. The $(1 - \mathcal{T}_a^D)$ factor is the above-cloud emissivity and B_a is the Planck function for a mean temperature of the emitting layer above the cloud.

A good way to measure the effect of the water vapor transmission on the sensitivity is to take the ratio of the affected sensitivity to the prototype sensitivity. This ratio of sensitivities is

$$\frac{\Delta I\uparrow_{\text{obs}}}{\Delta I\uparrow_{\text{proto}}} = \mathcal{T}_o\left[1 - \frac{I_t\downarrow}{I\uparrow_{\text{clr}}}\right] = \mathcal{T}_o\left[1 - (1 - \mathcal{T}_a^D)\frac{B_a}{I\uparrow_{\text{clr}}}\right]. \tag{A8}$$

If the transmission above the cirrus cloud is significantly less than unity, then the cirrus cloud is low enough so that the temperature of the emitting layer above the cirrus layer will be approximately the same as the effective radiative temperature of the atmosphere below, so $B_a \approx I_{\text{clr}}\uparrow$. This results in the approximation that the sensitivity is reduced according to

$$\frac{\Delta I\uparrow_{\text{obs}}}{\Delta I\uparrow_{\text{proto}}} = \mathcal{T}_o\mathcal{T}_a^D. \tag{A9}$$

If the observation altitude is above most of the water vapor, then the two transmissions are the same for the nadir view, and the ratio of the transmission-affected sensitivity to the true sensitivity is $\mathcal{T}_a^{1+D}$.

REFERENCES

Deeter, M. N., and K. F. Evans, 1997: Mesoscale variations of water vapor inferred from the millimeter-wave imaging radiometer during TOGA COARE. *J. Appl. Meteor.*, **36,** 183–188.

Draine, B., and J. Goodman, 1993: Beyond Clausius-Mossotti: Wave propagation on a polarizable point lattice and the discrete dipole approximation. *Astrophys. J.*, **405,** 685–697.

——, and P. J. Flatau, 1994: Discrete-dipole approximation for scattering calculations. *J. Opt. Soc. Amer. A,* **11,** 1491–1499.

Evans, K. F., and G. L. Stephens, 1995a: Microwave radiative transfer through clouds composed of realistically shaped ice crystals. Part I: Single scattering properties. *J. Atmos. Sci.,* **52,** 2041–2057.

——, and ——, 1995b: Microwave radiative transfer through clouds composed of realistically shaped ice crystals. Part II: Remote sensing of ice clouds. *J. Atmos. Sci.,* **52,** 2058–2072.

——, S. J. Walter, and W. R. McGrath, 1996: Submillimeter-wave radiometric sensing of cirrus cloud properties: The JPL prototype cloud ice radiometer. Preprints, *Eighth Conf. on Satellite Meteorology and Oceanography,* Atlanta, GA, Amer. Meteor. Soc., 357–361.

Fowler, L. D., D. Randall, and S. Rutledge, 1996: Liquid and ice cloud microphysics in the CSU general circulation model. Part I: Model description and simulated microphysical processes. *J. Climate,* **9,** 489–529.

Gasiewski, A. J., 1992: Numerical sensitivity analysis of passive EHF and SMMW channels to tropospheric water vapor, clouds, and precipitation. *IEEE Trans. Geosci. Remote Sens.,* **30,** 859–870.

Goedecke, G. H., and S. G. O'Brien, 1988: Scattering by irregular inhomogeneous particles via the digitized Green's function algorithm. *Appl. Opt.,* **27,** 2431–2437.

Heymsfield, A., 1972: Ice crystal terminal velocities. *J. Atmos. Sci.,* **29,** 1348.

——, and C. M. R. Platt, 1984: A parameterization of the particle size spectrum of ice clouds in terms of the ambient temperature and the ice water content. *J. Atmos. Sci.,* **41,** 846–855.

Kikuchi, K., 1968: On snow crystals of bullet type. *J. Meteor. Soc. Japan,* **46,** 128–132.

Klett, J. D., 1995: Orientation model for particles in turbulence. *J. Atmos. Sci.,* **52,** 2276–2285.

Kosarev, A. L., and I. P. Mazin, 1989: Empirical model of physical structure of the upper level clouds of the middle latitudes. *Radiation Properties of Cirrus Clouds*, E. Feigelson, Ed., Nauka, 29–52.

Larson, H. J., 1982: *Introduction to Probability Theory and Statistical Inference.* John Wiley and Sons, 637 pp.

Liebe, H. J., 1989: MPM—An atmospheric millimeter wave propagation model. *Int. J. Infrared Millimeter Waves*, **10,** 631–650.

Liou, K.-N., 1986: Influence of cirrus clouds on weather and climate processes. *Mon. Wea. Rev.*, **114,** 1167–1199.

Matrosov, S. Y., B. W. Orr, R. A. Kropfli, and J. B. Snider, 1994: Retrieval of vertical profiles of cirrus cloud microphysical parameters from Doppler radar and IR radiometer measurements. *J. Appl. Meteor.*, **33,** 617–626.

McFarquhar, G. M., and A. J. Heymsfield, 1996: Microphysical characteristics of three anvils sampled during the central equatorial pacific experiment. *J. Atmos. Sci.*, **53,** 2401–2423.

Mitchell, D. L., 1994: A model predicting the evolution of ice particle size spectra and radiative properties of cirrus clouds. Part I: Microphysics. *J. Atmos. Sci.*, **51,** 797–815.

Muller, B. M., H. E. Fuelberg, and X. Xiang, 1994: Simulations of the effects of water vapor, cloud liquid water, and ice on AMSU moisture channel brightness temperatures. *J. Appl. Meteor.*, **33,** 1133–1154.

Ono, A., 1969: The shape and riming properties of ice crystals in natural clouds. *J. Atmos. Sci.*, **26,** 138.

Platt, C. M. R., 1981: The effect of cirrus of varying optical depth on the extraterrestrial net radiative flux. *Quart. J. Roy. Meteor. Soc.*, **106,** 671–678.

——, N. L. Abshire, and G. T. McNice, 1978: Some microphysical properties of an ice cloud from lidar observation of horizontally oriented crystals. *J. Appl. Meteor.*, **17,** 1220–1224.

Racette, P., R. F. Adler, J. R. Wang, A. J. Gasiewski, D. M. Jackson, and D. S. Zacharias, 1996: An airborne millimeter-wave imaging radiometer for cloud, precipitation, and atmospheric water vapor studies. *J. Atmos. Oceanic Technol.*, **13,** 610–619.

Rossow, W. B., and R. A. Schiffer, 1991: ISSCP cloud data products. *Bull. Amer. Meteor. Soc.*, **72,** 2–20.

Stephens, G. L., and P. J. Webster, 1981: Clouds and climate: Sensitivity of simple systems. *J. Atmos. Sci.*, **38,** 235–247.

Warren, S. G., 1984: Optical constants of ice from the ultraviolet to the microwave. *Appl. Opt.*, **23,** 1206–1225.

Winker, D., and M. Vaughan, 1994: Vertical distribution of clouds over Hampton, Virginia observed by lidar under the ECLIPS and FIRE ETO programs. *Atmos. Res.*, **34,** 117–133.

Wylie, D. P., W. P. Menzel, H. M. Woolf, and K. I. Strabala, 1994: Four years of global cirrus cloud statistics using HIRS. *J. Climate*, **7,** 1972–1986.